Milling Bifurcations: A Review of Literature and Experiment

Andrew Honeycutt
Department of Mechanical Engineering and Engineering Science,
University of North Carolina at Charlotte,
Charlotte, NC 28223
e-mail: ahoney15@uncc.edu

Tony L. Schmitz
Department of Mechanical Engineering and Engineering Science,
University of North Carolina at Charlotte,
Charlotte, NC 28223
e-mail: tony.schmitz@uncc.edu

*This review paper presents a comprehensive analysis of period-*n *(i.e., motion that repeats every n tooth periods) bifurcations in milling. Although period-n bifurcations in milling were only first reported experimentally in 1998, multiple researchers have since used both simulation and experiment to study their unique behavior in milling. To complement this work, the authors of this paper completed a three year study to answer the fundamental question "Is all chatter bad?", where time-domain simulation and experiments were combined to: predict and verify the presence of period-2 to period-15 bifurcations; apply subharmonic (periodic) sampling strategies to the automated identification of bifurcation type; establish the sensitivity of bifurcation behavior to the system dynamics, including natural frequency and damping; and predict and verify surface location error (SLE) and surface roughness under both stable and period-2 bifurcation conditions. These results are summarized. To aid in parameter selection that yields period-*n *behavior, graphical tools including Poincaré maps, bifurcation diagrams, and stability maps are presented.* [DOI: 10.1115/1.4041325]

Keywords: milling, dynamics, stability, chatter, bifurcation, surface location error, surface roughness, time-domain simulation

1 Introduction

Milling, or subtractive material removal using a rotating tool with defined cutting edges (teeth), may be described by a system of second-order, time-delay differential equations with inertial, damping, and stiffness terms, as well as an external periodic forcing function defined by the force required to shear away material in the form of thin chips. A fundamental nonlinearity also exists because the tool/part vibration can grow to a level where a tooth leaves the cut when it would otherwise be engaged and the cutting force subsequently drops to zero.

Due to the time delay, various bifurcations (i.e., the appearance of a qualitatively different solution as a control parameter is varied) are exhibited. These bifurcations include: (1) secondary Hopf instability (traditional chatter); and (2) period-*n* motions (e.g., a period-2, flip, or period doubling bifurcation). Operating under secondary Hopf bifurcation conditions is avoided due to the large tool and/or workpiece motions and cutting forces and, subsequently, poor workpiece surface finish, part accuracy, and potential damage to the workpiece-tool-spindle system. In this review, however, a new question is posed. *Can milling under period-n bifurcation conditions at axial depths of cut that exceed the traditional (secondary Hopf) stability limit be leveraged to achieve higher material removal rates, while still satisfying part accuracy and surface finish requirements?* To answer this question, a three-year systematic study that incorporated both time-domain simulation and experiments was completed to comprehensively explore period-*n* bifurcation behavior in milling.

The paper is organized as follows: First, background information on the significant prior work in milling stability and period-*n* bifurcations is summarized. Second, the time-domain simulation and experimental setups for the three-year study are described. Third, period-*n* behavior is detailed, including the periodic sampling strategy, Poincaré maps, bifurcation diagrams, and stability maps. Fourth, predictions and experiments for surface location error (SLE) and surface roughness under both stable and period-2 bifurcation conditions are presented. Finally, conclusions are provided.

Manuscript received January 16, 2018; final manuscript received August 27, 2018; published online October 5, 2018. Assoc. Editor: Satish Bukkapatnam.

2 Background

Analytical and numerical modeling of milling operations has enjoyed a rich history. During the mid19th century, self-excited vibrations that can occur during milling were first described using time-delay differential equations [1,2]. The feedback mechanism (i.e., the time delay term) was defined as "regeneration of waviness," where the previously cut surface combined with the instantaneous vibration state dictates the current chip thickness, force level, and corresponding vibration response [3–6]. This work resulted in frequency-domain, analytical algorithms that were used to produce the now well-known stability lobe diagram that separates the spindle speed-chip width domain into regions of stable and unstable behavior [5–18]; see Fig. 1.

In 1998, Davies et al. used once per revolution sampling to characterize the synchronicity of cutting tool motions with the tool rotation in milling [19]. They observed the traditional secondary Hopf bifurcation [20], as well as period-3 tool motion (i.e., motion that repeated with a period of three cutter revolutions) during partial radial immersion milling. In 2000, Davies et al. further

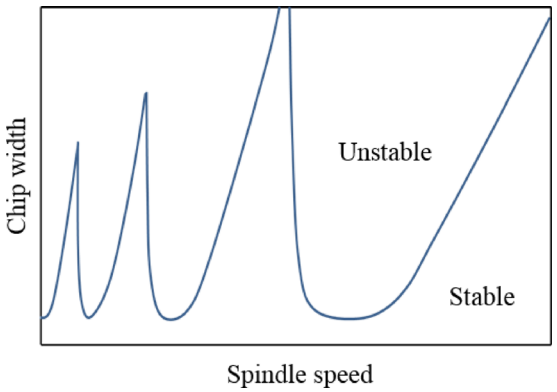

Fig. 1 Example stability lobe diagram. Stable and unstable zones are separated by the stability boundary (or limit). The control parameters are chip width, or axial depth of cut in milling, and spindle speed, which defines the forcing frequency and time delay between teeth.

examined the stability of highly interrupted machining [21] by developing a two-stage map to describe: (1) noncutting motions governed by an analytical solution; and (2) motions during cutting using an approximation (fixed tool position with a change in momentum). They reported a doubling of the number of optimally stable spindle speeds when the time in cut is small. Experiments confirmed the new, low radial immersion best speeds. Davies' work led to follow-on studies in milling bifurcations that included advanced simulation strategies and new process insights.

In 2001, Moon and Kalmár-Nagy reviewed the "prediction of complex, unsteady and chaotic dynamics" in machining [20]. They listed the various contributors to nonlinear behavior, including the loss of tool-workpiece contact due to large amplitude vibration and workpiece material constitutive relations, and highlighted previous applications of nonlinear dynamics methods to the study of chatter [22–27]. They also specified the use of phase-space methods, such as Poincaré maps, to identify changes in machining process dynamics.

Time-domain simulation has been used extensively to study milling behavior [28,29]. For example, Zhao and Balachandran implemented time-domain simulation, which incorporated the loss of tool-workpiece contact and regeneration, to study the process dynamics [30]. They identified secondary Hopf bifurcation and suggested that "period-doubling bifurcations are believed to occur" for low radial immersions. They included bifurcation diagrams for limited axial depth of cut ranges at two spindle speeds to demonstrate the two bifurcation types.

Davies et al. extended their initial work in 2002 to present the first analytical stability boundary for highly interrupted machining [31]. It was based on modeling the cutting process as a kicked harmonic oscillator with a time delay and followed the two-stage map concept described in Ref. [21]. They used the frequency content of a microphone signal to establish the existence of both secondary Hopf and period-2 instabilities. Mann et al. also provided experimental validation of secondary Hopf and period-2 instabilities for up and down milling [32]. They reported "a kind of period triple phenomenon" observed using the once per revolution sampled displacement signal recorded from a single degree-of-freedom (SDOF) flexure-based machining platform.

The semidiscretization, time finite element analysis, and multi-frequency methods were also developed to produce milling stability charts that predict both instabilities [33–37]. In Ref. [38], it was shown using the semidiscretization method that the period-2 bifurcation exhibits closed curves within the secondary Hopf lobes, except for the highest speed stability lobe. Simultaneous secondary Hopf (quasi-periodic) and period-2 bifurcation behavior was also observed. It was reported that this "combination" behavior occurred at unstable axial depths of cut above the period-2 lobes. Additionally, period-3 behavior was seen and it was noted that this "periodic chatter" with period-3 (or higher) always occurred above a secondary Hopf stability limit. The same group [39] reported further experimental evidence of secondary Hopf, period-2, -3, -4, and combined secondary Hopf and period-2 chatter, depending on the spindle speed-axial depth values for a two degree-of-freedom dynamic system. Budak and Altintas presented a multi-frequency solution for the stability boundary that also predicts period-2 behavior [40,41]. A comparison of the multi-frequency and semidiscretization methods is presented in Ref. [42].

A perturbation analysis was performed in Ref. [43] to identify the secondary Hopf and period-2 bifurcations and increase the parameter space exploration efficiency. Additionally, numerical integration was implemented to construct a bifurcation diagram for a selected spindle speed that demonstrated the transition from stable operation to quasi-periodic chatter as the axial depth is increased. Stépán et al. continued to explore the nonlinear aspects of milling behavior in 2005 [44]. They described stable period-2 motion where the tool does not contact the workpiece in each tooth period (even in the absence of runout). For a two flute cutter, for example, only one tooth contacts the workpiece per revolution; they referred to this condition as the "fly over effect" and included a bifurcation diagram for these proposed stable and unstable period-2 oscillations.

The effect of the helix angle on period-2 behavior was studied by Zatarain et al. [45]. They found that, depending on the helix angle, the closed curves within the secondary Hopf lobes change their size and shape. They also found that these closed islands of stability can appear even in the highest speed stability lobe (in contrast to the results when helix angle is not considered). This work was continued in Ref. [46], where the authors showed that at axial depths equal to the axial pitch of the cutter teeth, the equation of motion becomes an autonomous delay differential equation so the period-2 behavior is not possible. Patel et al. studied the helix effect in up and down milling using the time finite element approach in Ref. [47]. Bobrenkov et al. used the time finite element and Chebyshev collocation methods to investigate the influence of simultaneously engaged teeth on milling bifurcations [48]. It was observed that multiple teeth engagement with three or more teeth yielded smaller period-2 regions.

In recent work, Moradi et al. included tool wear and process damping in the bifurcation analysis of milling behavior [49]. Cheng et al. presented a reconstructed vibration signal in state space for ultra precision machining [50]. Honeycutt and Schmitz presented "extended milling bifurcation diagrams" that revealed higher order period-n bifurcations at depths of cut well above the traditional stability limit [51]. Period-n bifurcations were predicted and experimentally validated for milling in Refs. [52] and [53]. A new metric was described that automatically differentiates between stable and unstable behavior of different types for time-domain simulation of the milling processes [54,55]. The approach was based on periodic sampling of milling signals at once per tooth period, τ, and integer multiples of the tooth period, $n\tau$.

3 Time-Domain Simulation and Experimental Setup

3.1 Time-Domain Simulation. Time-domain simulation enables the numerical solution of the coupled, time delay equations of motion for milling in small time steps. It is well suited to incorporating all the intricacies of milling dynamics, including the nonlinearity that occurs if the tooth leaves the cut due to large amplitude vibrations and complicated tool geometries (including runout, or different radii, of the cutter teeth, nonproportional teeth spacing, and variable helix). The simulation is based on the regenerative force, dynamic deflection model described by Smith and Tlusty [28]. As opposed to stability maps that provide a global picture of the stability behavior, time-domain simulation provides information regarding the local cutting force and vibration behavior (at the expense of computational efficiency) for the selected cutting conditions. The simulation used in this study proceeds as follows (see Fig. 2):

(1) the instantaneous chip thickness is determined using the vibration of the current and previous teeth at the selected tooth angle
(2) the cutting force components in the tangential (t) and normal (n) directions are calculated using

$$\begin{aligned} F_t(t) &= k_{tc} b h(t) + k_{te} b \\ F_n(t) &= k_{nc} b h(t) + k_{ne} b \end{aligned} \tag{1}$$

where b is the axial depth of cut, $h(t)$ is the instantaneous chip thickness, and the cutting force coefficients are identified by the subscripts t or n for direction and c or e for cutting or edge effect.
(3) the force components are used to find the new displacements by numerical solution of the differential equations of motion in the x (feed) and y directions:

$$\begin{aligned} m_x \ddot{x} + c_x \dot{x} + k_x x &= F_t(t)\cos\phi + F_n(t)\sin\phi \\ m_y \ddot{y} + c_y \dot{y} + k_y y &= F_t(t)\sin\phi - F_n(t)\cos\phi \end{aligned} \tag{2}$$

where m is the modal mass, c is the modal viscous damping coefficient, and k is the modal stiffness. The subscripts identify the direction and multiple degrees of freedom in each direction can be accommodated.

(4) the tool rotation angle is incremented and the process is repeated.

The instantaneous chip thickness depends on the nominal, tooth angle-dependent chip thickness, the current vibration in the direction normal to the surface, and the vibration of previous teeth at the same angle. The chip thickness can be expressed using the circular tooth path approximation as:

$$h(t) = f_t \sin\phi + n(t-\tau) - n(t) \tag{3}$$

where f_t is the commanded feed per tooth, ϕ is the tooth angle, n is the normal direction (see Fig. 2), and τ is the tooth period. The tooth period is defined as

$$\tau = \frac{60}{\Omega N_t}(\text{s}) \tag{4}$$

where Ω is the spindle speed in rpm and N_t is the number of teeth. The vibration in the direction of the surface normal for the current tooth depends on the x and y vibrations as well as the tooth angle according to:

$$n = x\ \sin\phi - y\ \cos\phi \tag{5}$$

For the simulation, the strategy is to divide the angle of the cut into a discrete number of steps. At each small time-step, dt, the cutter angle is incremented by the corresponding small angle, $d\phi$. This approach enables convenient computation of the chip thickness for each simulation step because: (1) the possible teeth orientations are predefined; and (2) the surface created by the previous teeth at each angle may be stored. The cutter rotation

$$d\phi = \frac{360}{\text{SR}}(\text{deg}) \tag{6}$$

depends on the selection of the number of steps per revolution, SR. The corresponding time-step is

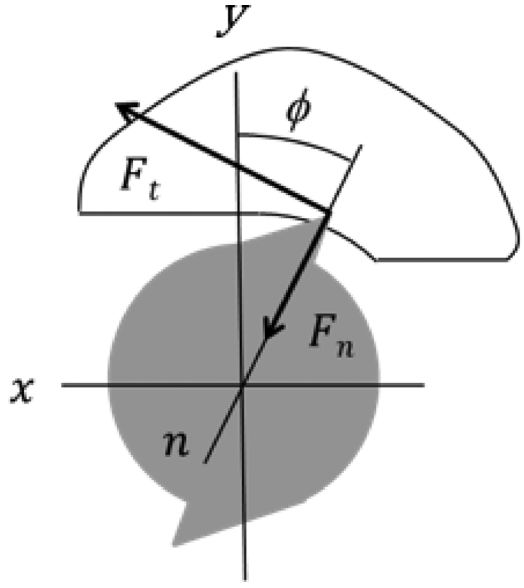

Fig. 2 Milling simulation geometry. The normal and tangential direction cutting forces, F_n and F_t, are identified. The fixed *x* and *y* directions, as well as the rotating normal direction, *n*, are also shown. The angle ϕ defines the tooth angle. The tool feed is to the right for the clockwise tool rotation and the axial depth is in the *z* direction.

$$dt = \frac{60}{\text{SR}\Omega}(\text{s}) \tag{7}$$

A vector of angles is defined to represent the potential orientations of the teeth as the cutter is rotated through one revolution of the circular tool path, $\phi = [0,\ d\phi,\ 2\ d\phi,\ 3\ d\phi,\ \ldots,\ (\text{SR}-1)\ d\phi]$. The locations of the teeth within the cut are then defined by referencing entries in this vector.

In order to accommodate the helix angle for the tool's cutting edges, the tool may be sectioned into a number of axial slices. Each slice is treated as an individual straight tooth end mill, where the thickness of each slice is a small fraction, db, of the axial depth of cut, b. Each slice incorporates a distance delay

$$r\chi = db\ \tan\gamma \tag{8}$$

relative to the prior slice (nearer the cutter free end), which becomes the angular delay between slices

$$\chi = \frac{db\ \tan\gamma}{r} = \frac{2db\ \tan\gamma}{d}(\text{rad}) \tag{9}$$

for the rotating end mill, where d is the end mill diameter and γ is the helix angle. In order to ensure that the angles for each axial slice match the predefined tooth angles, the delay angle between slices is

$$\chi = d\phi \tag{10}$$

This places a constraint on the db value. By substituting $d\phi$ for χ and rearranging, the required slice width is

$$db = \frac{d(d\phi)}{2\tan\gamma} \tag{11}$$

This simple description can be extended to include:

(1) multiple tool modes—the x and y forces are used to calculate the acceleration, velocity, and displacement for each tool mode (represented by the modal parameters) and the results are summed in each direction

(2) flexible workpiece—the x and y forces are also used to determine the workpiece deflections, again by numerical integration, and the relative tool-workpiece vibration is used to calculate the instantaneous chip thickness

(3) runout of the cutter teeth—the chip thickness is updated by the runout of the current tooth

(4) unequal teeth spacing—the tooth angle vector is modified to account for the actual tooth pitch.

Using this time-domain simulation approach [55], the forces, displacements, and velocities may be calculated. These results are then sampled once-per-tooth period to generate Poincaré maps, bifurcation diagrams, and stability maps.

3.2 Experimental Setup. Experiments were completed using a SDOF flexure to define the system dynamics, where the SDOF flexure was much less stiff than the cutting tool [32]. The flexure setup (see Fig. 3) also simplified the measurement instrumentation. The flexure motions were measured using a Lion Precision DMT20 capacitance probe (CP) (displacement), Polytec OFV-5000 laser vibrometer (LV) (velocity), and PCB 352C23 low mass piezoelectric accelerometer (acceleration). In order to enable once-per-tooth sampling of the vibration signals, a laser tachometer (LT) was used. A small section of reflective tape was attached to the tool holder and the corresponding (digital) tachometer signal was used to perform the periodic sampling.

4 Period-*n* Bifurcations

4.1 Periodic Sampling. In milling, the tooth period (and therefore the time delay) is defined by the spindle speed and

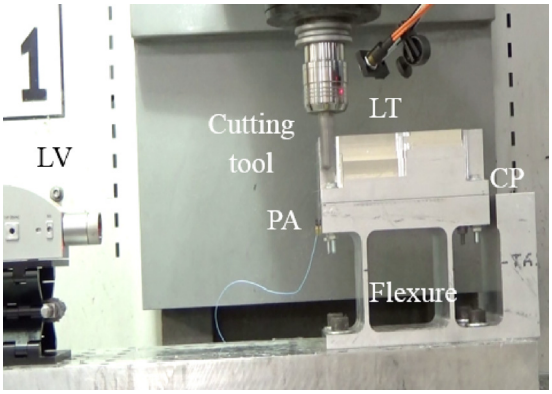

Fig. 3 Milling experimental setup with instrumentation including a LV, piezo-accelerometer, LT, and CP. The setup was located on a Haas TM-1 CNC milling machine.

number of teeth; see Eq. (4). To evaluate the process performance, the time-domain signals may be sampled at the tooth period (i.e., once-per-tooth sampling). If the once-per-tooth sampled points repeat, the response is periodic with the forcing function and the process is stable. If not, the character of the once-per-tooth sampled points can be used to identify the bifurcation type. To complete this evaluation visually, a Poincaré map can be used.

4.2 Poincaré Maps. In this work, Poincaré maps were constructed using both experiments and simulations. For the experiments, the displacement and velocity of a flexible workpiece (the tool dynamic stiffness was much higher) were recorded using a capacitance probe and laser vibrometer and then sampled once-per-tooth period using a laser tachometer. In simulation, the displacement and velocity were predicted, but the same sampling strategy was applied. By plotting the displacement versus velocity, the phase space trajectory could be observed in both cases. The once-per-tooth period samples were then superimposed and used to interrogate the milling process behavior.

For stable cuts, the motion is periodic with the tooth period, so the sampled points repeat and a single grouping of points is observed. When secondary Hopf instability occurs, the motion is quasi-periodic with tool rotation because the chatter frequency is (generally) incommensurate with the tooth passing frequency. In this case, the once-per-tooth sampled points do not repeat and they form an elliptical distribution. For a period-2 bifurcation, the motion repeats only once every other cycle (i.e., it is a subharmonic of the forcing frequency). In this case, the once-per-tooth sampled points alternate between two solutions. For period-n bifurcations, the sampled points appear at n distinct locations in the Poincaré map.

To demonstrate these behaviors, Figs. 4–9 are included. For a selected milling system, the spindle speed was varied for fixed radial and axial depths of cut. Figures 4 and 5 show the time domain response and Poincaré map for stable conditions (forced vibration). It is observed that the once-per-tooth sampled points repeat with each tooth passage in this case.

Figures 6 and 7 demonstrate a period-2 bifurcation. At the new spindle speed, the behavior repeats every other tooth passage. This yields alternating points in the time domain plot and two sets of points in the Poincaré map.

Figures 8 and 9 display the results for a secondary Hopf bifurcation. The introduction of the new chatter frequency (in addition to the tooth passing frequency) provides an elliptical distribution of points in the Poincaré map for this quasi-periodic behavior.

4.3 Bifurcation Diagrams. In the bifurcation diagrams developed for this study, the once-per-tooth sampled displacement (vertical axis) was plotted against the axial depth of cut (horizontal axis). The transition in stability behavior from stable (at low axial depths) to period-n or secondary Hopf instability (at higher axial depths) is then directly observed. This diagram represents the information from multiple Poincaré maps over a range of axial depths, all at a single spindle speed. A stable cut appears as a single point (i.e., the sampled points repeat when only forced vibration is present). A period-2 bifurcation, on the other hand, appears as a pair of points offset from each other in the vertical direction. This represents the two collections of once-per-tooth sampled points from the Poincaré map. A secondary Hopf bifurcation is seen as a vertical distribution of points; this represents the range of once-per-tooth sampled displacements from the elliptical distribution of points in the Poincaré map.

4.4 Stability Maps. Stability maps, or stability lobe diagrams, identify the limiting axial depth of cut (vertical axis) as a function of spindle speed (horizontal axis). Traditionally, this limit is represented as a single contour which separates stable (forced vibration only) from unstable (secondary Hopf or period-n) parameter combinations. This map provides a global view of the stability behavior, but does not, in general, identify the type of instability. Because a bifurcation diagram presents the stability behavior as a function of axial depth, but only at one spindle speed, it can be considered as a high fidelity vertical slice of a stability map. Conversely, a stability map can be interpreted as a series of bifurcation diagrams where a binary switching function is used to categorize the behavior represented by the vertical distribution of once-per-tooth sampled points as either stable or unstable.

4.5 Period-n Numerical and Experimental Results. In this section, comparisons are made between time-domain simulation predictions and milling experiments for period-n bifurcations using multiple flexures. The cutting tool was a 19.1 mm diameter, single flute carbide square end mill (30 deg helix angle). Modal impact testing verified that the cutting tool dynamic stiffness (1055 Hz natural frequency, 0.045 viscous damping ratio, and 4.2×10^7 N/m stiffness for a single mode fit) was much higher than the SDOF flexure. Cutting tests were completed using Fig. 3 setup. The measured flexure dynamics and cutting conditions are listed in Table 1. Each cut of the 6061-T6 aluminum workpiece was performed using a feed per tooth of 0.10 mm/tooth. The aluminum alloy cutting force coefficients were: $k_{tc} = 792 \times 10^6$ N/m^2, $k_{nc} = 352 \times 10^6$ N/m^2, $k_{te} = 26 \times 10^3$ N/m, and $k_{ne} = 28 \times 10^3$ N/m.

A bifurcation diagram for a spindle speed of 3800 rpm and radial depth of 5 mm was predicted by simulation and then cuts were performed from 1 mm to 7 mm axial depths in 0.5 mm steps. The capacitance probe displacement signal was sampled using the laser tachometer to construct an experimental bifurcation diagram. Figures 10–17 provides the comparison between prediction and experiment. For this axial depth of cut range, period-3 bifurcations were observed (see the period-3 entry from Table 1 for the flexure dynamics).

A simulated stability map for the same axial depth of cut range as Fig. 17, but spindle speeds from 3300 rpm to 4300 rpm is displayed in Fig. 18 (the same dynamics were again used). The diagram was constructed by completing time-domain simulations over a grid with a spindle speed resolution of 10 rpm and an axial depth resolution of 0.1 mm.

To construct the stability map using time-domain simulation results, a separate simulation was completed at each position in the selected grid of spindle speed and axial depth values. A primary challenge in this approach, however, is automatically establishing the stability limit using the predicted time domain signals. As described in Ref. [54], a stability criterion based on the once-per-tooth sampled data was implemented. The stability metric was

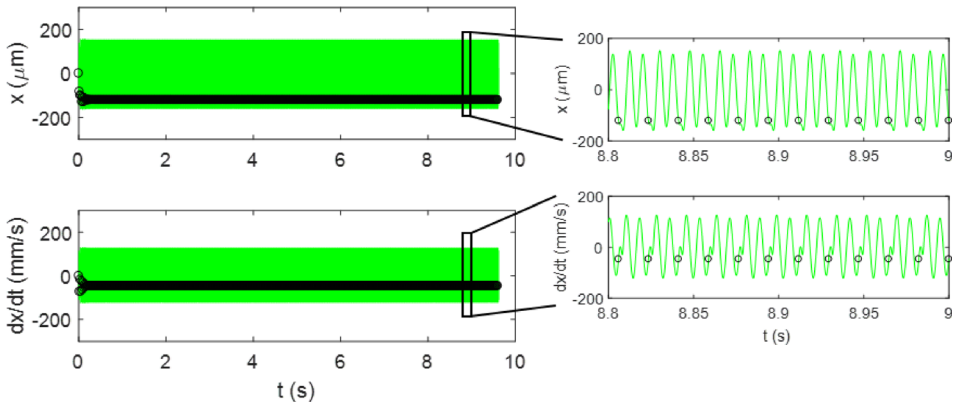

Fig. 4 Time domain results for a stable cut (3400 rpm). (Top) time-dependent displacement with periodic samples (circles); (bottom) time-dependent velocity with periodic samples. (Inset) higher magnification view to observe individual periodic samples of the displacement (top) and velocity (bottom).

$$M1 = \frac{\sum_{i=2}^{N} \left| x_{s1}(i) - x_{s1}(i-1) \right|}{N} \tag{12}$$

where x_{s1} is the vector of once-per-tooth sampled x displacements and N is the length of the x_{s1} vector. Other variables, such as y displacement or cutting force could be selected as well. With this stability metric, the absolute value of the differences in successive sampled points is summed and then normalized. The sampled points repeat for a stable cut, so the $M1$ value is ideally zero. For unstable cuts, on the other hand, $M1 > 0$, due to the asynchronous motion in secondary Hopf instability and jumps from one fixed point to the next in period-n bifurcations.

The initial transients were removed and the $M1$ value for each simulation was calculated (see Eq. (12)). An arbitrarily small value of 1 μm was selected to differentiate between stable and unstable parameter combinations; this contour is shown in Fig. 18 and identifies the stability limit. The transition from stable to unstable behavior at 3800 rpm observed in Fig. 17 is replicated. The transition from secondary Hopf to period-3 to secondary Hopf seen in the bifurcation diagram is not detailed in the stability map, however. This limitation is addressed in Sec. 4.7.

4.6 Period-*n* Bifurcation Sensitivity to System Dynamics. Table 1 shows that different bifurcation behavior was obtained for varying flexure dynamics. This suggests that the system dynamics play a critical role in the period-n behavior that is obtained. To explore this sensitivity, additional experiments were performed.

A first set of experiments was completed to demonstrate the sensitivity of the period-n bifurcation behavior to natural frequency. During the cutting trials, material was removed from the workpiece. This lowered the workpiece mass and, subsequently, increased the flexure's natural frequency. Since the mass of the chips is much smaller than the workpiece, this material removal resulted only in small changes in natural frequency. The variation in system dynamics for the results presented in Figs. 19–22 is provided in Table 2. The higher period-n bifurcations exhibited sufficient sensitivity to flexure natural frequency that, within a single cut, both period-n bifurcation and quasi-periodic behavior (secondary Hopf bifurcation) were observed. For these tests, the cutting tool was a 19.1 mm diameter, single flute carbide square end mill (30 deg helix angle). The cutting tool dynamic response was: 1055 Hz natural frequency, 0.045 viscous damping ratio, and 4.2×10^7 N/m stiffness. Each cut of the 6061-T6 aluminum workpiece was performed using a feed per tooth of 0.10 mm/tooth. The aluminum alloy cutting force coefficients were: $k_{tc} = 792 \times 10^6$ N/m^2, $k_{nc} = 352 \times 10^6$ N/m^2, $k_{te} = 26 \times 10^3$ N/m, and $k_{ne} = 28 \times 10^3$ N/m.

Figures 19–22 display the flexure's feed direction velocity (dx/dt) in the time domain. The continuous signal is displayed as a solid line, while the circles are the once-per-tooth sampled points. In each figure, the left plot shows the simulated behavior and the right plot shows the experimental behavior. Good agreement is observed. The time-domain simulation was modified to account for the changing natural frequency due to mass loss. After each time-step, the change in mass was calculated based on the volume of the removed chip and the density of the workpiece material (2700 kg/m^3). This change in mass was then used to update the flexure's natural frequency for the next time-step.

A summary of the behavior seen in Figs. 19–22 is provided here.

(1) Figure 19 exhibits period-6 behavior from 4 to 11 s, followed by quasi-periodic behavior until the end of the cut.
(2) Figure 20 shows period-6 behavior from 4 to 13 s and then quasi-periodic behavior is observed until the end of the cut.
(3) Figure 21 displays quasi-periodic behavior from the beginning of the cut until 11 s and then period-7 behavior from 11 to 15 s.
(4) Figure 22 exhibits quasi-periodic behavior from the beginning of the cut until 8 s, period-15 behavior from 8 to 13 s, and then quasi-periodic behavior until the end of the cut.

In addition to the changes in bifurcation behavior with natural frequency, the sensitivity to damping was evaluated in a second

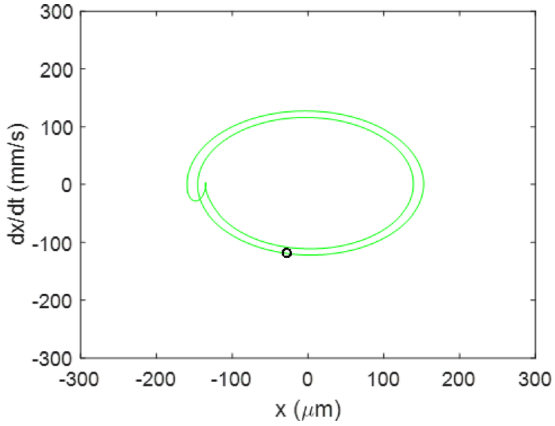

Fig. 5 Poincaré map for stable cut (3400 rpm). The sampled points align at a single location for the forced vibration case.

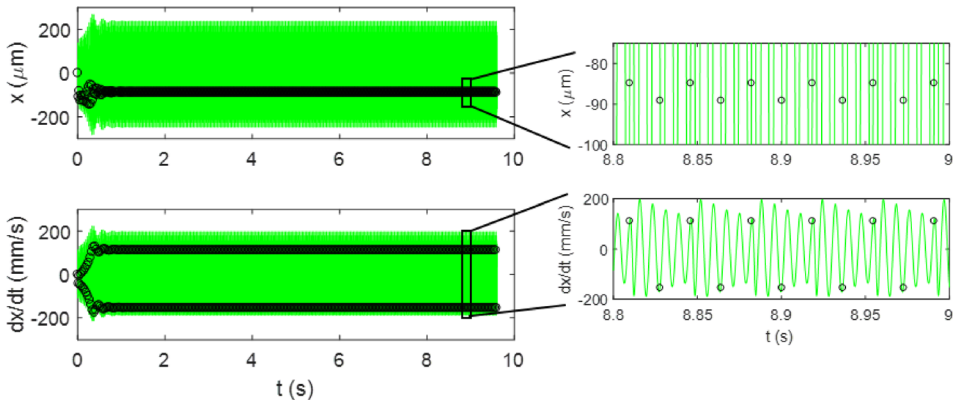

Fig. 6 Time domain results for a period-2 bifurcation (3310 rpm)

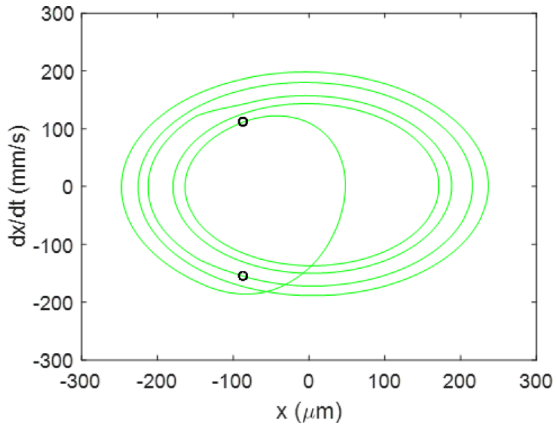

Fig. 7 Poincaré map for period-2 bifurcation (3310 rpm). The sampled points align at a two fixed locations for the period-2 bifurcation.

set of tests. In order to vary the experimental damping, the flexure-based setup displayed in Fig. 3 was replaced with a second flexure to enable adjustable viscous damping. The approach was to add an eddy current damper to the flexure as described in Ref. [52]; see Fig. 23. In the figure, it is seen that a copper conductor is attached to the moving platform. As the conductor moves through the magnetic field generated by the permanent magnets (PM) located on each side, a velocity-dependent force is produced, which opposes the motion. The effect is viscous damping that can be increased or decreased by changing the gap between the conductor and magnets.

To explore the sensitivity of period-n behavior to damping, machining trials were conducted over a range of axial depths of cut (1 mm–10 mm) with four different flexure damping values. In all cases, the spindle speed was 3310 rpm, the radial depth of cut was 2 mm, and the feed per tooth was 0.1 mm/tooth. The cutting tool was a 19.1 mm diameter, single flute carbide square end mill (30 deg helix angle): 1055 Hz natural frequency, 0.045 viscous damping ratio, and 4.2×10^7 N/m stiffness. The 6061-T6 aluminum alloy cutting force coefficients were: $k_{tc} = 792 \times 10^6$ N/m^2, $k_{nc} = 352 \times 10^6$ N/m^2, $k_{te} = 26 \times 10^3$ N/m, and $k_{ne} = 28 \times 10^3$ N/m. Table 3 details the tunable flexure dynamics for the four damping values.

Simulated and experimental bifurcation diagrams are presented in Figs. 24–27 for the dynamics defined in Table 3. It is observed that as the damping increases, the region of period-2 behavior diminishes in size and, in Fig. 27 with a damping ratio of 3.55%, it disappears all together. The stable behavior persists up to an axial depth of approximately 4 mm for Figs. 24–27. The period-2 behavior is then seen for decreasing ranges of axial depth as the damping increases. It continues to approximately 8.2 mm for 1.47%, to approximately 7.6 mm for 1.91%, and to approximately 6.8 mm for 2.34%. In all cases, the period-2 behavior is followed by a second stable zone at higher axial depths.

To observe the global behavior, stability maps were generated using the same time domain simulation implemented to construct Figs. 24–27. The spindle speed range was 2600 rpm to 3800 rpm in steps of 20 rpm and the axial depth range was 0.2 mm to 10 mm in steps of 0.2 mm. The results are presented in Fig. 28, where a vertical line is added to each panel at 3310 rpm to indicate the

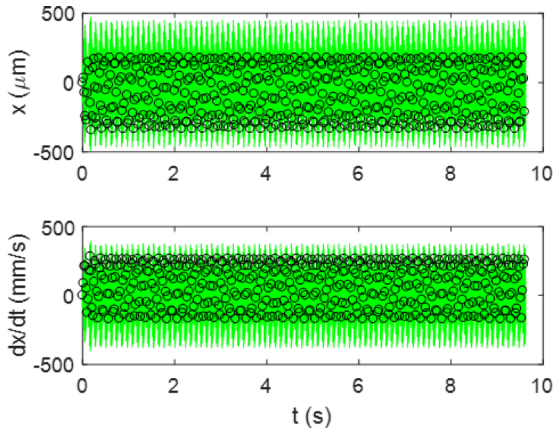

Fig. 8 Time domain results for a secondary Hopf bifurcation (2850 rpm)

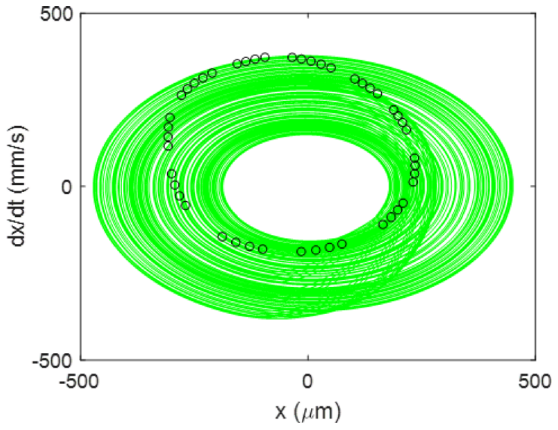

Fig. 9 Poincaré map for secondary Hopf bifurcation (2850 rpm). The sampled points are arranged in an elliptical distribution.

Table 1 Cutting conditions and flexure dynamics for experiments

	Cutting conditions			Flexure dynamics		
Period-n (figure number)	Spindle speed (rpm)	Axial depth, b (mm)	Radial depth (mm)	Stiffness (N/m)	Natural frequency (Hz)	Viscous damping ratio (%)
2 (10)	3486	2.0	1.0	9.0×10^5	83.0	2.00
3 (11)	3800	4.5	5.0	5.6×10^6	163.0	1.08
6 (12)	3200	18.0	1.0	5.6×10^6	202.6	0.28
6 (13)	3250	15.5	1.0	5.6×10^6	205.8	0.28
7 (14)	3200	14.5	1.0	5.6×10^6	204.1	0.28
8 (15)	3310	15.0	2.0	2.1×10^6	130.1	1.47
15 (16)	3200	14.0	1.0	5.6×10^6	204.8	0.28

position of the bifurcation diagrams in Figs. 24–27. The stability metric defined in Eq. (12) was used to identify stable and unstable conditions for each grid point.

4.7 Subharmonic Sampling. As shown in Fig. 18, the $M1$ stability metric defined in Eq. (12) does not seperately identify secondary Hopf and period-n bifurcations. However, using subharmonic sampling at $n\tau$ ($n = 2, 3, 4, \ldots$), the corresponding period-n bifurcations can be separately established [55]. For example, when sampling at 2τ, the stability metric becomes "blind" to period-2 bifurcations. By sampling at every other tooth passage (2τ), the period-2 behavior appears as synchronous motion (stable). The same is true for period-3 bifurcations if the sampling interval is 3τ, and so on.

Considering the same dynamic system used for Fig. 18 (period-3 experimental setup from Table 1), a simulation was performed for a spindle speed of 4070 rpm at an axial depth of 3.6 mm. This is within the unstable island in Fig. 18. The time history and Poincaré map are displayed in the top row of Fig. 29 for once-per-tooth sampling. A period-2 bifurcation is observed. The $M1$ value is 106.7 μm for the period-2 bifurcation; this value was calculated from the flexure (workpiece) x direction displacement for the final 75 tooth periods of a 750 tooth period simulation. The bottom row shows the results for 2τ subharmonic sampling. The metric for this case is

$$M2 = \frac{\sum_{i=2}^{N} \left| x_{s2}(i) - x_{s2}(i-1) \right|}{N} \tag{13}$$

where x_{s2} is the vector of x displacements sampled once every other tooth period (i.e., a 2τ sampling period), and N is the length of the x_{s2} vector. It is observed that the cut now appears to be stable; the $M2$ value is 1.2×10^{-9} μm $\cong$ 0. Generically, the metric can be expressed as shown in Eq. (14), where the integer $n = 1, 2, 3, \ldots$ defines the sampling period (i.e., $n\tau$)

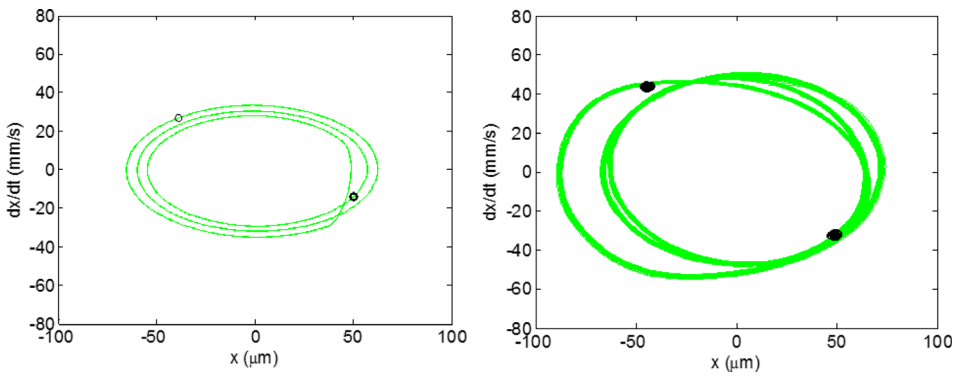

Fig. 10 Poincaré map for period-2 bifurcation. (Left) simulation, (right) experiment. The phase space trajectory is represented by the solid line and the once-per-tooth sampled points are displayed as circles.

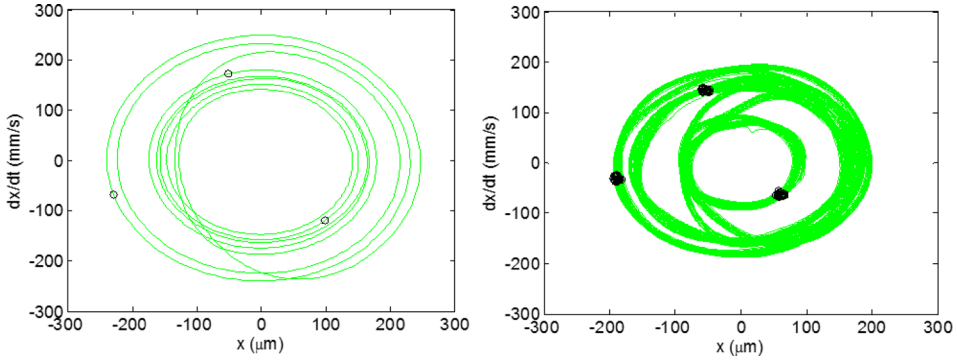

Fig. 11 Poincaré map for period-3 bifurcation. (Left) simulation, (right) experiment.

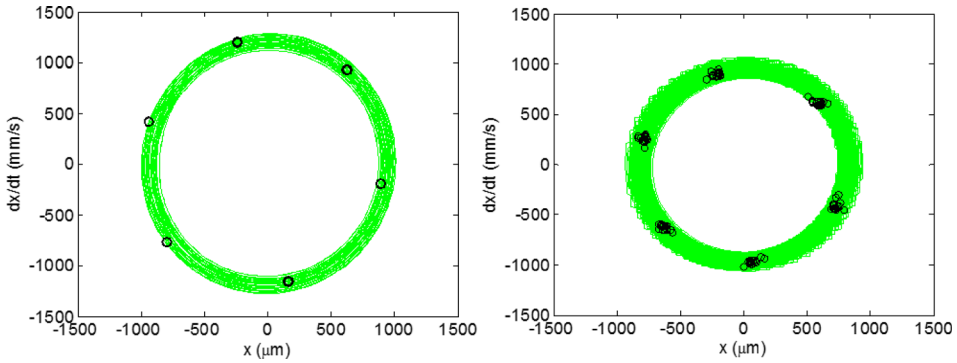

Fig. 12 Poincaré map for period-6 bifurcation. (Left) simulation, (right) experiment.

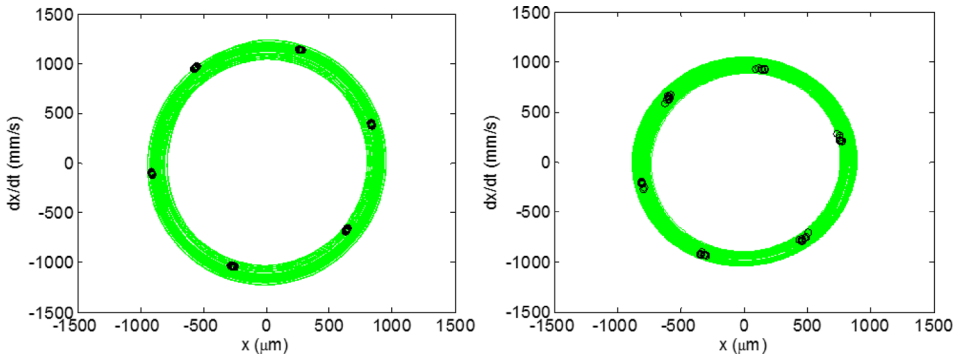

Fig. 13 Poincaré map for a second period-6 bifurcation. (Left) simulation, (right) experiment.

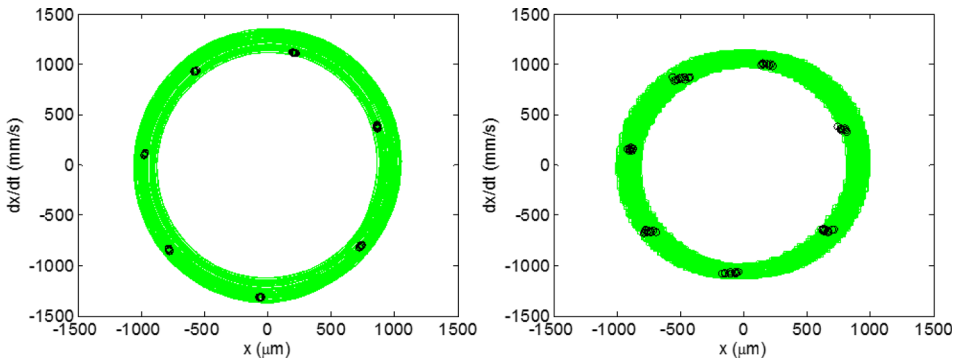

Fig. 14 Poincaré map for period-7 bifurcation. (Left) simulation, (right) experiment.

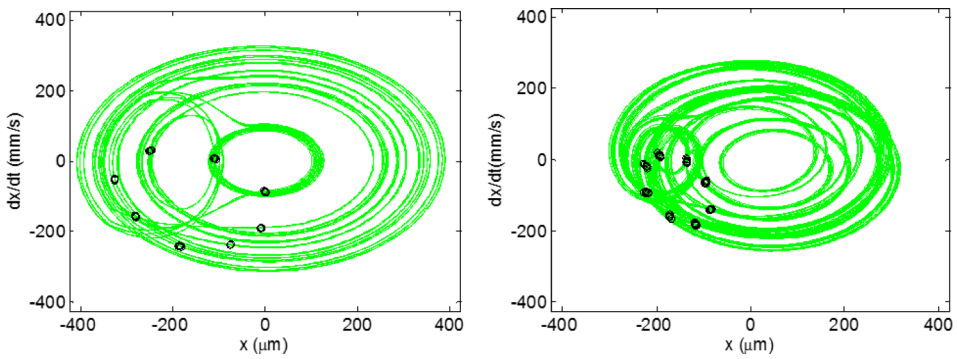

Fig. 15 Poincaré map for period-8 bifurcation. (Left) simulation, (right) experiment.

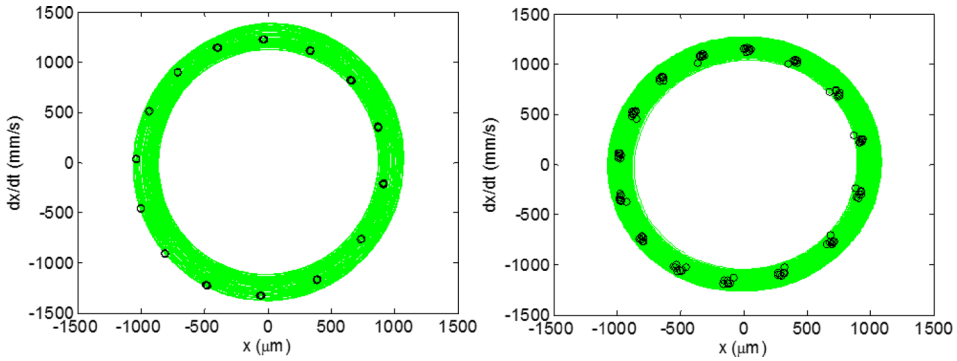

Fig. 16 Poincaré map for period-15 bifurcation. (Left) simulation, (right) experiment.

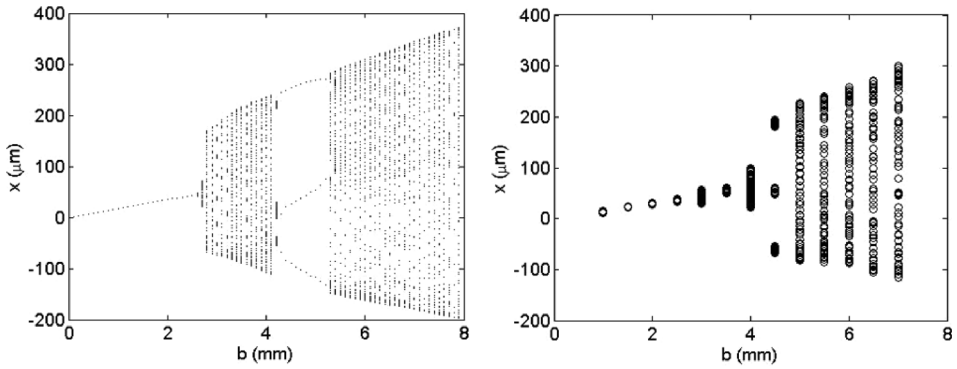

Fig. 17 Bifurcation diagram for 3800 rpm and 5 mm radial depth of cut. (Left) simulation, (right) experiment.

$$Mn = \frac{\sum_{i=2}^{N} \left| x_{sn}(i) - x_{sn}(i-1) \right|}{N} \tag{14}$$

Next, the stability map shown in Fig. 12 was developed using $n\tau$ sampling with $n = 1$, 2, 3, and 4. These results are provided in Fig. 30. In panel a), once per tooth sampling (τ sampling period) was applied to calculate $M1$ using Eq. (12). A single contour is plotted at $M1 = 1$ μm. For panel b), the sampling period is 2τ. It is seen that the unstable island no longer appears. This follows from Fig. 29, where it is seen that the 2τ sampling is blind to period-2 bifurcations. A single contour is plotted at $M2 = 1$ μm according to Eq. (13). In panel (c), 3τ sampling is applied. The period-2 bifurcation zone re-appears as seen panel (a), but a new "stable" zone is also visible. This is the region of period-3 bifurcations that is was not previously visible with the once-per-tooth sampling approach. Panel (d) displays the results for 4τ sampling. The period-2 bifurcations are again eliminated because 2τ is a factor of 4τ. However, a new stable band also appears to the left of the period-3 bifurcation zone in panel c). This new band identifies period-4 bifurcations and would not have been discovered without subharmonic sampling. In panels (c) and (d), the stability metric (Eqs. (12) and (13)) was updated to accommodate the new sampling periods and a single contour at a metric value of 1 μm was plotted.

The subharmonic sampling approach is now implemented to construct a stability map that individually identifies each bifurcation type. The metrics $M1$ through $M7$, which represent τ through 7τ integer sampling periods, are used to isolate the stable zone as well as the different bifurcation types: period-2, -3, -4, -5, -6, -7, and secondary Hopf. The logic used to construct the stability map follows:

if $M1 \leq 1$ μm
  (stable, do nothing)
elseif $M2 \leq 1$ μm
  plot a circle (period-2)
elseif $M3 \leq 1$ μm
  plot a triangle (period-3)
elseif $M4 \leq 1$ μm and $M2 > 1$ μm
  plot a square (period-4, excludes period-2)
elseif $M5 \leq 1$ μm

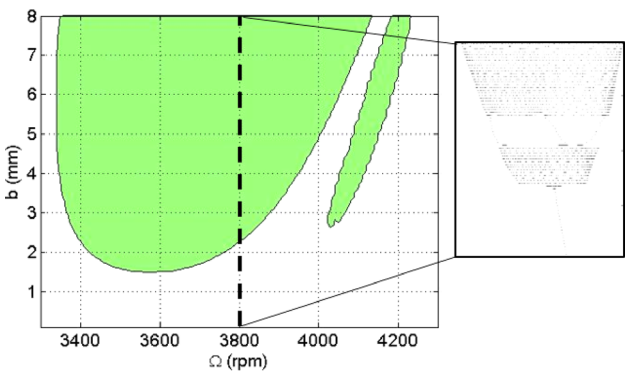

Fig. 18 Simulated stability map for period-3 experimental setup from Table 1 ($M1 = 1$ μm contour). The transition from stable to unstable behavior occurs at approximately 2.6 mm for a spindle speed of 3800 rpm. The inset shows the bifurcation diagram progression at 3800 rpm from stable to quasi-periodic instability to period-3 and back to quasi-periodic behavior.

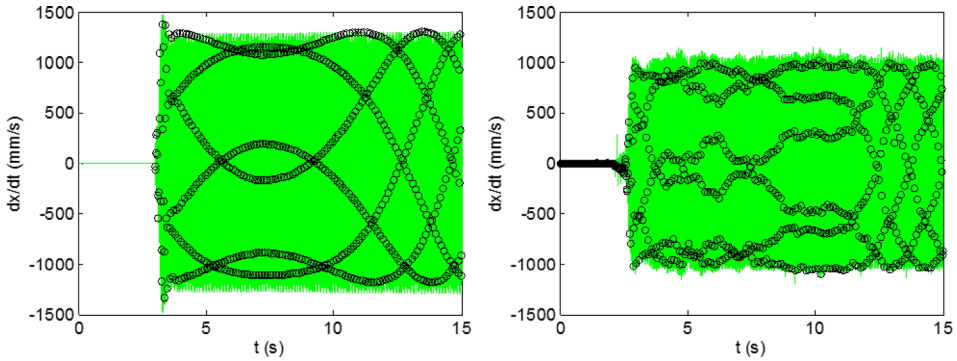

Fig. 19 Variation in bifurcation behavior with changes in natural frequency. The natural frequency changes with time as more material is removed. Period-6 bifurcation is observed. (Left) simulation, (right) experiment.

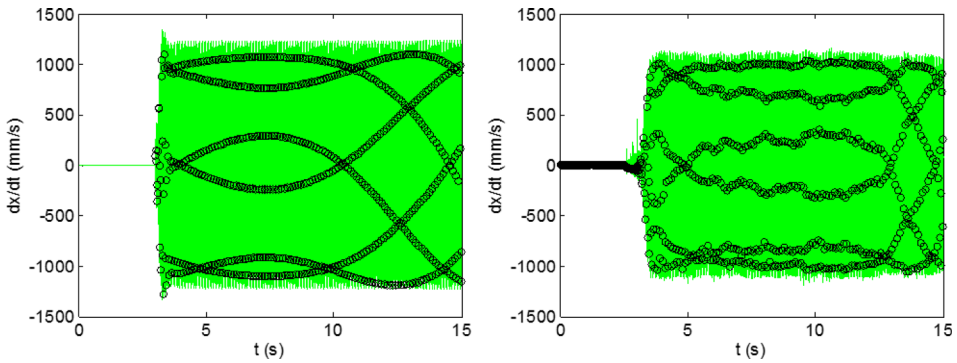

Fig. 20 Variation in bifurcation behavior with changes in natural frequency. Period-6 bifurcation is observed. (Left) simulation, (right) experiment.

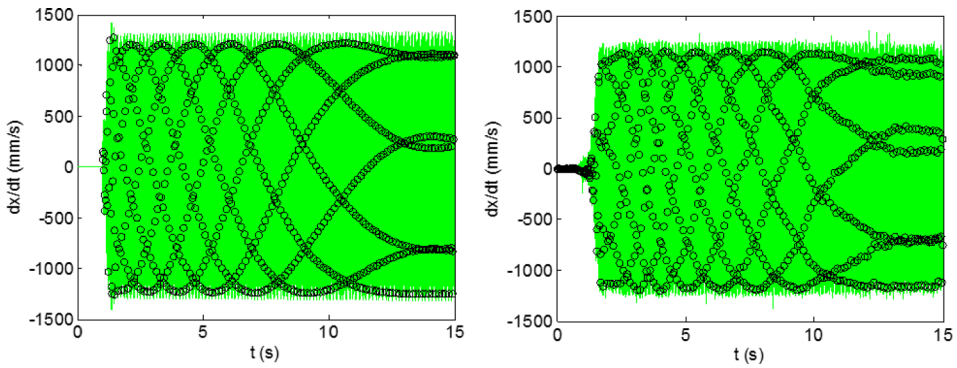

Fig. 21 Variation in bifurcation behavior with changes in natural frequency. Period-7 bifurcation is observed. (Left) simulation, (right) experiment.

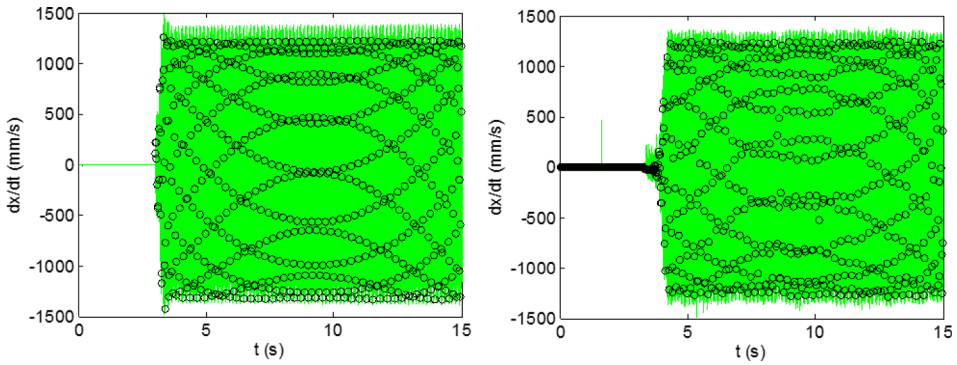

Fig. 22 Variation in bifurcation behavior with changes in natural frequency. Period-15 bifurcation is observed. (Left) simulation, (right) experiment.

Table 2 Changes in flexure natural frequency due to mass removal

	Flexure dynamics				Cutting conditions		
Period-n (figure number)	Natural frequency, beginning of cut (Hz)	Natural frequency, end of cut (Hz)	Change in natural frequency (Hz)	Change in mass (g)	Spindle speed (rpm)	Axial depth, b (mm)	Radial depth (mm)
6 (19)	202.4	202.7	0.3	4.8	3200	18.0	1.0
6 (20)	205.7	205.9	0.2	4.1	3250	15.5	1.0
7 (21)	204.1	204.3	0.2	3.9	3200	14.5	1.0
15 (22)	204.7	204.9	0.2	3.7	3200	14.0	1.0

plot a + (period-5)elseif $M6 \leq 1$ μm and $M2 > 1$ μm and $M3 > 1$ μm
plot a diamond (period-6, excludes period-2 and period-3)
elseif $M7 \leq 1$ μm
plot an × (period-7)
else
plot a dot (secondary Hopf or high order period-n)
end

The result is displayed in Fig. 31. The stable zone is the open white area and the various instabilities are indicated by the symbols. The box in the figure indicates the spindle speed range and axial depth (6.4 mm) for the bifurcation diagram in Fig. 32. By following the bifurcations in the map from period-2 (circle), to -3 (triangle), to -4 (square), to -5 (+), to -6 (diamond), to -7 (×), it appears that a pattern is emerging. Within the single stability lobe, the increasing order shifts the period-n zones to progressively lower spindle speeds. Also, the size of the zones diminishes with increasing order. The period numbers for the various zones are provided above the stability map. For period-5 and -7 bifurcations, there are additional zones; these are denoted by parenthetical order numbers in Fig. 31. There is one extra zone for period-5 and two for period-7.

For the SDOF dynamic systems explored here, the spindle speeds for the period-n bifurcations can be expressed analytically. The derivation is based on the "best speeds," $\Omega_{\text{best},j}$ (rpm), equation available from the analytical milling stability analysis [54], where f_n is the natural frequency (Hz) corresponding to the most flexible vibration mode and $j = 1, 2, 3, \ldots$.

$$\Omega_{\text{best},j} = \frac{60 f_n}{j N_t} \tag{15}$$

In this equation, j is the stability lobe number and orders the stability lobes in descending spindle speeds. For example, $j = 1$ is the rightmost lobe in the stability map. For the period-n bifurcation speeds above the jth best speed ($j \geq 2$), the corresponding expression is

$$\Omega_{\text{period}-n,j} = \Omega_{\text{best},j} + \left(\frac{\Omega_{\text{best},j-1} - \Omega_{\text{best},j}}{n} \right) \tag{16}$$

Substituting for $\Omega_{\text{best},j}$ and $\Omega_{\text{best},j-1}$ from Eq. (15) and simplifying gives:

$$\Omega_{\text{period}-n,j} = \frac{60 f_n}{N_t} \left(\frac{n(j-1)+1}{n(j-1)j} \right) \tag{17}$$

For the additional odd $n \geq 5$ bifurcation zones observed in Fig. 28, Eq. (16) is modified to be

$$\Omega_{\text{period}-n,j} = \Omega_{\text{best},j} + 2\left(\frac{\Omega_{\text{best},j-1} - \Omega_{\text{best},j}}{n} \right) \tag{18}$$

for the first extra zone ($n = 5$ and $n = 7$) and

$$\Omega_{\text{period}-n,j} = \Omega_{\text{best},j} + 3\left(\frac{\Omega_{\text{best},j-1} - \Omega_{\text{best},j}}{n} \right) \tag{19}$$

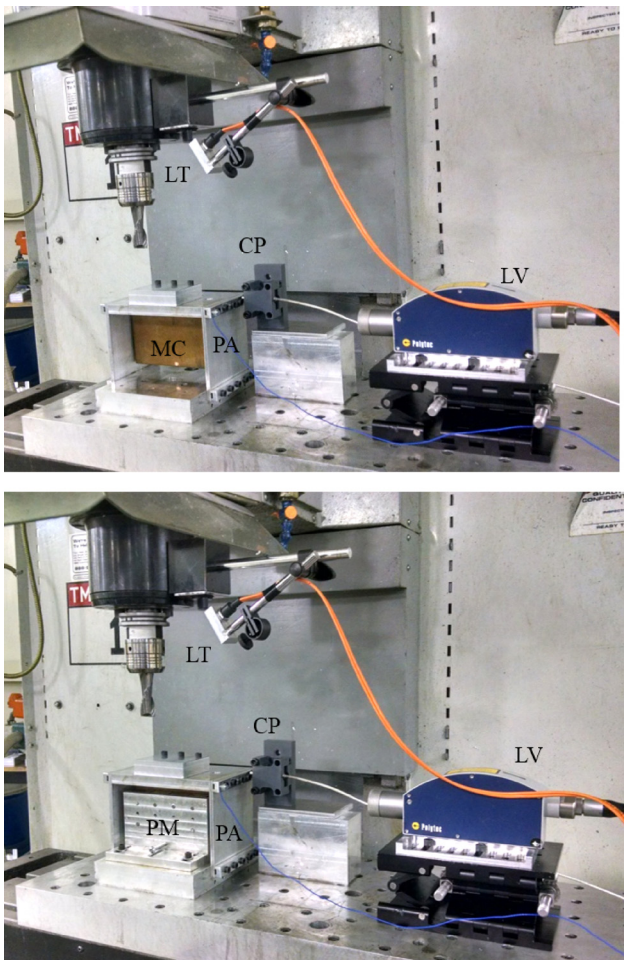

Fig. 23 Milling experimental setup with variable viscous damping. The setup includes a LV, piezo-accelerometer, LT, CP, moving conductor, and PM. The top photograph shows the flexure without the PM; the copper conductor is visible inside the parallelogram leaf-type flexure. The lower photograph shows the PM in place. The magnets are positioned on both sides of the copper conductor and provide the eddy current damping effect. The setup was located on a Haas TM-1 CNC milling machine.

Table 3 Flexure dynamics for damping sensitivity experiments

Period-n (figure number)	Stiffness (N/m)	Natural frequency (Hz)	Viscous damping ratio (%)
2 (24)	2.1×10^6	130.0	1.47
2 (25)	2.1×10^6	130.0	1.91
2 (26)	2.1×10^6	130.0	2.34
– (27)	2.1×10^6	130.0	3.55

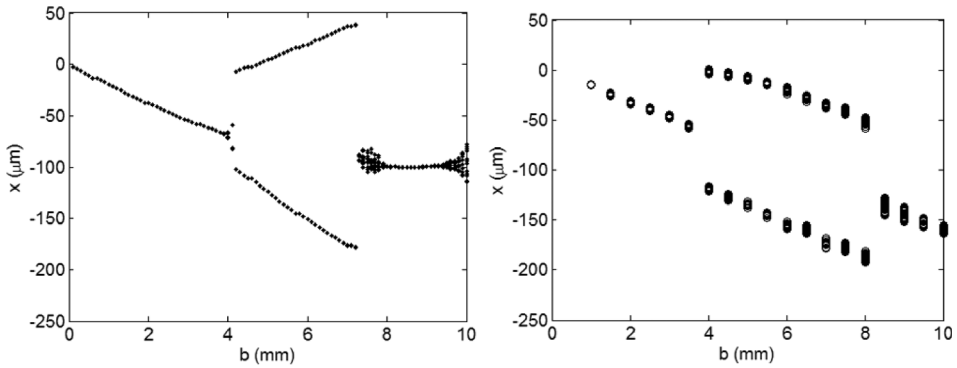

Fig. 24 Bifurcation diagram for 1.47% damping (3310 rpm). (Left) simulation, (right) experiment. Stable behavior is observed up to approximately 4 mm, period-2 behavior then occurs up to approximately 8 mm, then stable behavior is again seen.

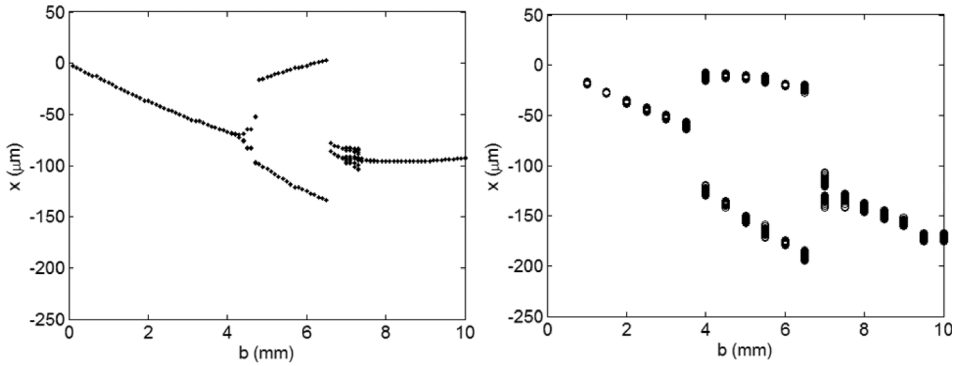

Fig. 25 Bifurcation diagram for 1.91% damping (3310 rpm). (Left) simulation, (right) experiment.

for the second extra zone ($n = 7$). Substituting Eq. (15) in Eq. (18) and simplifying gives

$$\Omega_{\text{period}-n,j} = \frac{60 f_n}{N_t}\left(\frac{n(j-1)+2}{n(j-1)j}\right) \tag{20}$$

Substituting Eq. (15) in Eq. (19) and simplifying yields

$$\Omega_{\text{period}-n,j} = \frac{60 f_n}{N_t}\left(\frac{n(j-1)+3}{n(j-1)j}\right) \tag{21}$$

The application of Eqs. 17, 20, and 21 to Fig. 31 ($f_n = 163$ Hz) is provided in Table 4. Considering $j = 3$ and the corresponding best speed of $(60 \cdot 163/13) = 3260$ rpm, the period-n bifurcation speeds were calculated.

5 Surface Location Error and Surface Roughness

When stable machining conditions are selected, two additional considerations for high quality part manufacture are: (1) SLE, or part geometric errors that occur due to forced vibrations; and (2) surface roughness. SLE has been modeled and predicted for stable milling conditions by several authors [36,56–70]. In these publications, the difference between the machined surface location and the commanded location is measured and/or predicted to determine the influence of (stable) machining conditions on the error. Similarly, surface roughness has been considered as an important

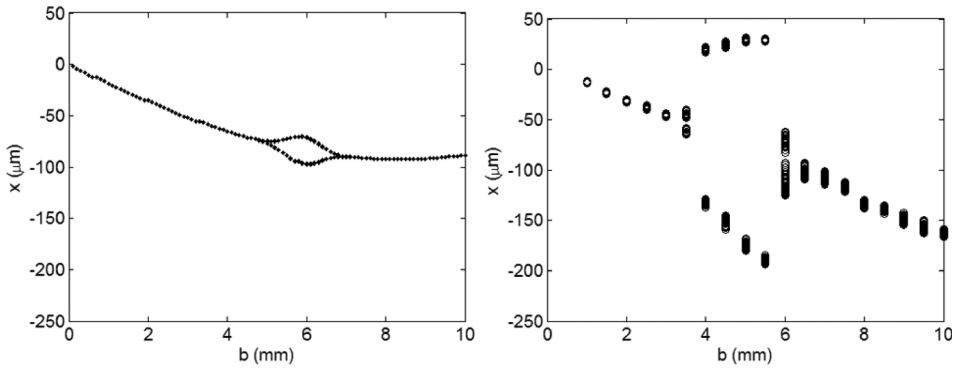

Fig. 26 Bifurcation diagram for 2.34% damping (3310 rpm). (Left) simulation, (right) experiment.

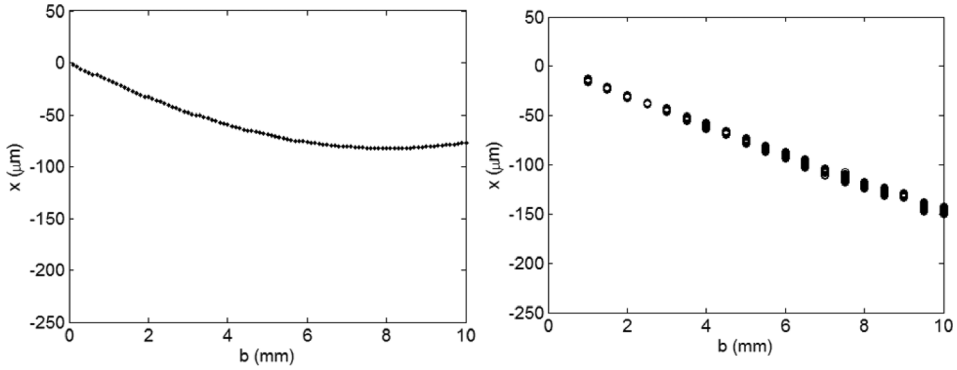

Fig. 27 Bifurcation diagram for 3.55% damping (3310 rpm). (Left) simulation, (right) experiment.

quality metric for machined parts since it influences fatigue, sealing performance, wear, and esthetics, for example. However, prior studies of period-n bifurcations (instabilities) have evaluated neither SLE nor surface roughness. The purpose of this section is to predict and measure both quantities for stable and period-2 bifurcation behaviors. Numerical and experimental results are presented for SLE and arithmetic average surface roughness, Ra, when milling under both stable and period-2 bifurcation conditions [71].

5.1 Time-Domain Simulation Modification. To complete SLE and Ra predictions, the time-domain simulation in Sec. 3.2 was augmented. Once the x and y direction displacements are determined, the final spatial trajectory for each tooth is determined by summing these vibration-induced displacements with the nominal cycloidal motion of the teeth due to the combined translation and rotation. This final spatial trajectory is used to define the machined surface and, subsequently, to predict the SLE and Ra. The nominal cycloidal motion components in the x and y directions are defined in Eqs. (22) and (23), where i is the time-step index and df is the linear feed per time-step (see Eq. (24))

$$x_{\text{nom}} = r\sin\phi + idf \tag{22}$$

$$y_{\text{nom}} = r\cos\phi \tag{23}$$

$$df = \frac{f_t N_t}{SR} \tag{24}$$

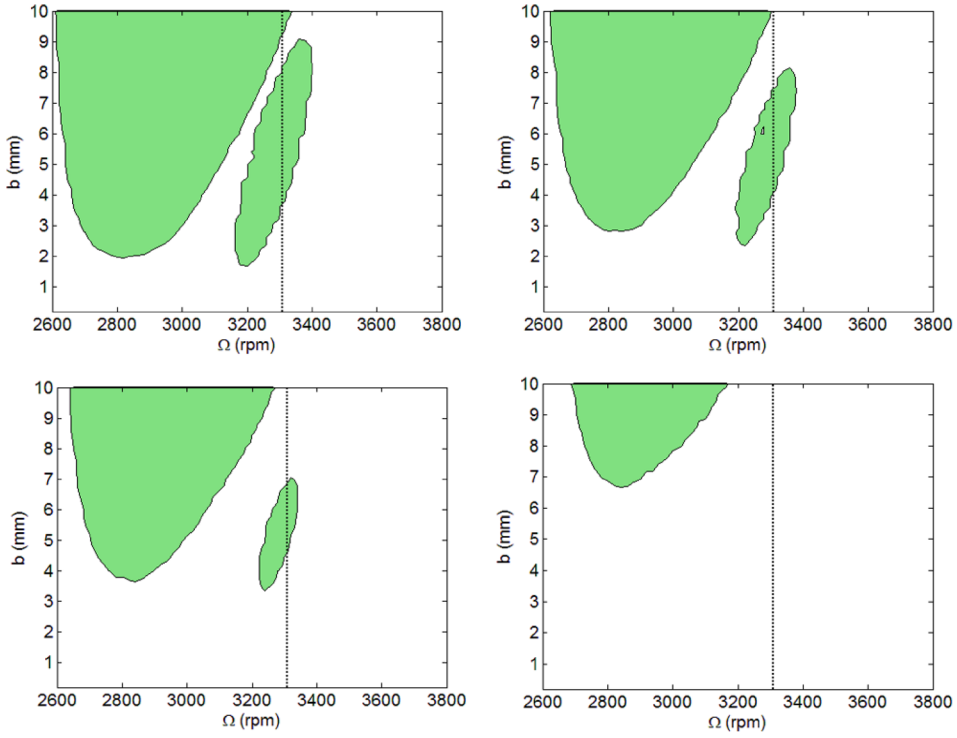

Fig. 28 Simulated stability maps for four damping levels ($M1 = 1$ μm contours). (Top left) 1.47% damping. As the axial depth is increased, the transition from stable to period-2 (3.8 mm), period-2 back to stable (8.2 mm), and stable to quasi-periodic behavior (9.2 mm) is observed. (Top right) 1.91% damping. As the axial depth is increased, the transition from stable to period-2 (4.2 mm) and period-2 back to stable (7.6 mm) occurs. (Bottom left) 2.34% damping. As the axial depth is increased, the transition from stable to period-2 (4.6 mm) and period-2 back to stable (6.8 mm) is observed. (Bottom right) 3.55% damping. Stable behavior is obtained at all axial depths.

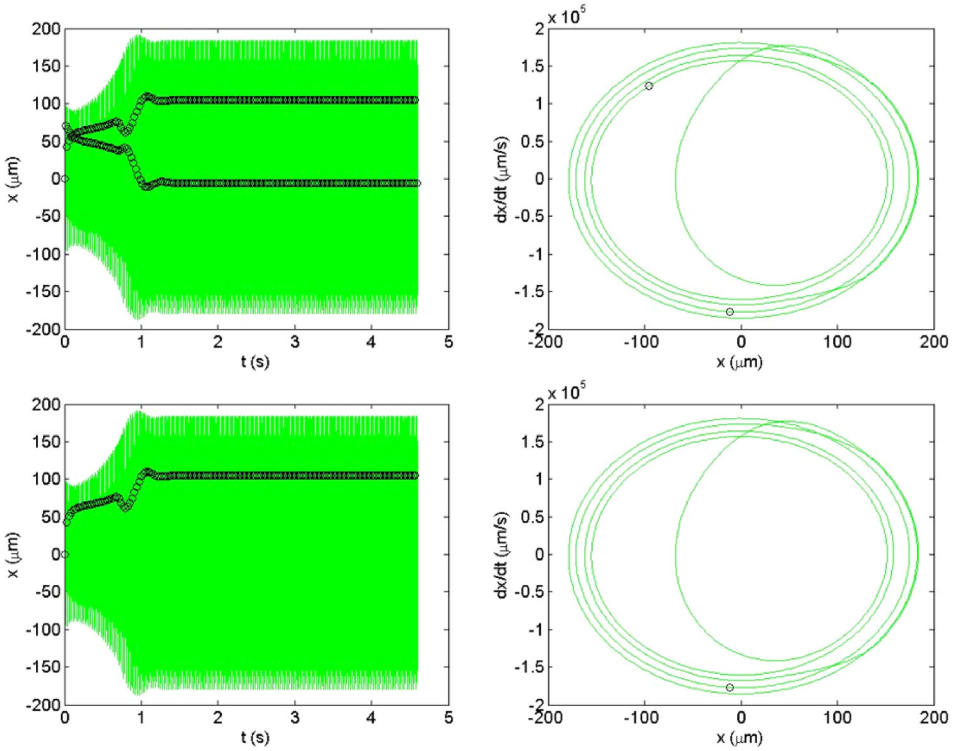

Fig. 29 Simulation results for a spindle speed of 4070 rpm at an axial depth of 3.6 mm. The workpiece *x* displacement and velocity are shown. (Top row) Time history (left) and Poincaré map (right) for once per tooth sampling (τ sampling period). (Bottom row) Time history (left) and Poincaré map (right) for subharmonic sampling at 2τ.

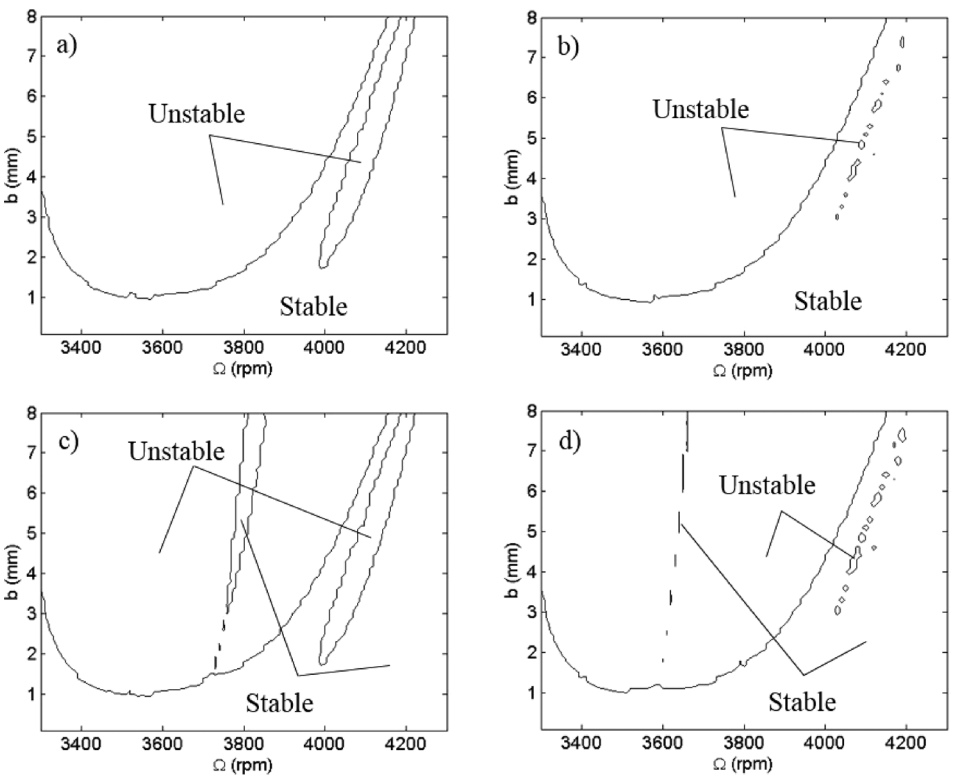

Fig. 30 (*a*) Once per tooth sampling (τ sampling period); (*b*) 2τ sampling period; (*c*) 3τ sampling period; and (*d*) 4τ sampling period. The zones that appear to be stable and unstable, depending on the sampling period, are marked.

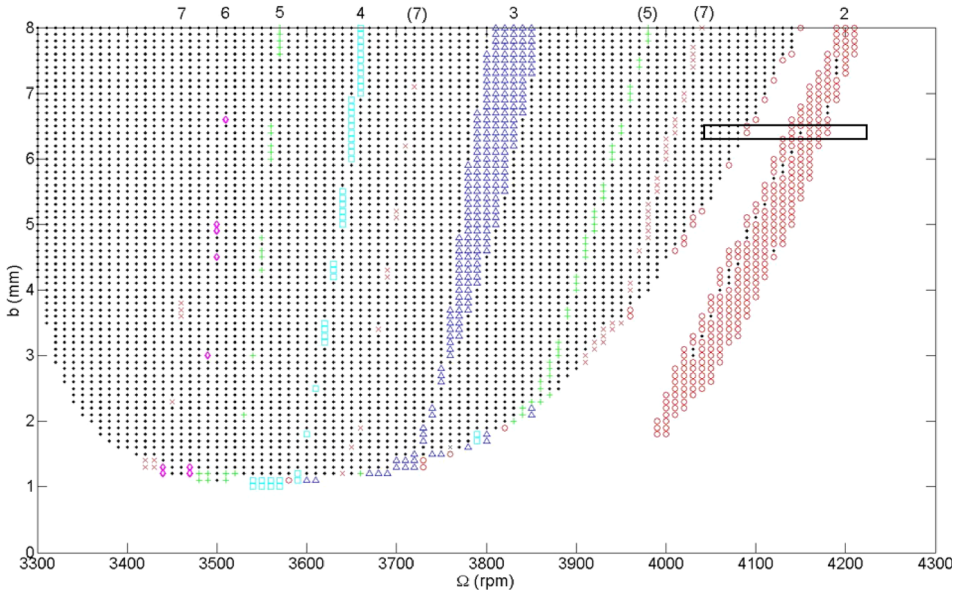

Fig. 31 New stability map. Period-2 (circle), period-3 (triangle), period-4 (square), period-5 (+), period-6 (diamond), period-7 (×), and secondary Hopf (dot) bifurcations are individually identified. The box indicates the spindle speed range and axial depth (6.4 mm) for the bifurcation diagram in Fig. 32.

5.2 Experimental Results. The flexure-based setup displayed in Fig. 33 was used to define a physical system for simulation and testing [32,72]. The setup included a parallelogram leaf-type flexure with an aluminum workpiece mounted on top. The in-process vibration data was collected using a Polytec OFV-5000 laser vibrometer (velocity) and Lion Precision DMT20 capacitance probe (displacement). Both were aligned with the flexible direction for the single degree-of-freedom flexure. Note that, unlike the prior stability testing, the feed direction is perpendicular to this flexible direction. This orientation was selected to emphasize variations in surface location error and surface finish with machining conditions. Once-per-tooth sampling was again accomplished using a laser tachometer and reflective target attached to the rotating tool holder. The flexure dynamics were identified by modal testing: 125.8 Hz natural frequency, 0.0136 viscous damping ratio, and 1.75×10^6 N/m stiffness in the flexible (feed) direction. The dynamics for the 19.1 mm diameter, 0 deg helix angle cutting tool (one insert) were symmetric: 1188 Hz natural frequency, 0.095 viscous damping ratio, and 4.24×10^7 N/m stiffness. The 6061-T6 aluminum alloy cutting force coefficients were: $k_{tc} = 770 \times 10^6$ N/m^2, $k_{nc} = 368 \times 10^6$ N/m^2, $k_{te} = 22 \times 10^3$ N/m, and $k_{ne} = 22 \times 10^3$ N/m. The up milling cutting conditions were: 5 mm axial depth, 2 mm radial depth, 0.35 mm/tooth, and variable

Table 4 Predicted period-*n* bifurcation speeds for Fig. 31 dynamic system

n	$\Omega_{\text{period}-n,3}$ (rpm)	First extra zone (rpm)	Second extra zone (rpm)
2	4075		
3	3803		
4	3668		
5	3586	3912	
6	3532		
7	3493	3726	3959

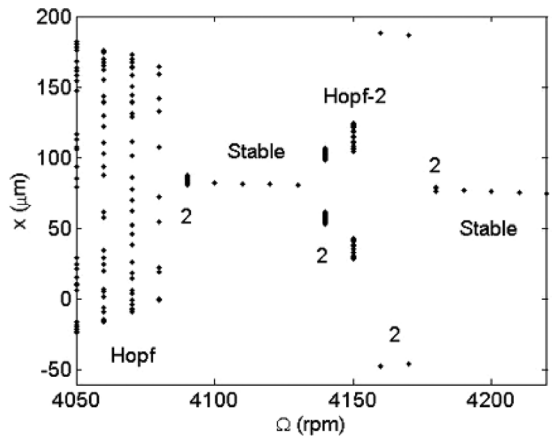

Fig. 32 Bifurcation diagram for an axial depth of 6.4 mm. Secondary Hopf (Hopf), period-2 (2), stable (Stable), and combination secondary Hopf and period-2 (Hopf-2) behaviors are specified.

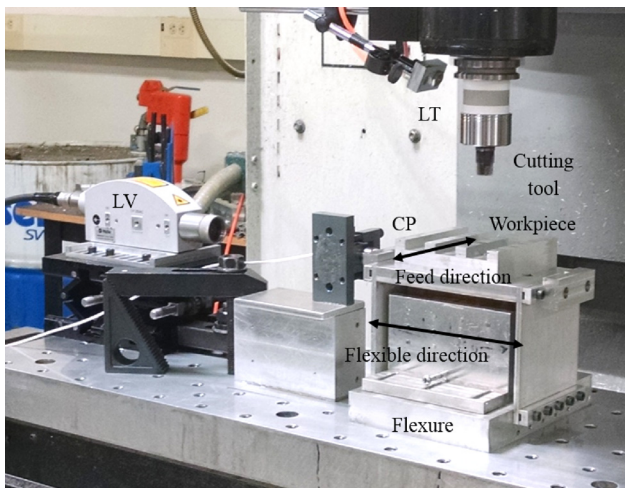

Fig. 33 Surface location error/Ra experimental setup with LV, LT, and CP. The feed direction and the flexible direction for the SDOF flexure are also identified. The setup was located on a Haas TM-1 CNC milling machine.

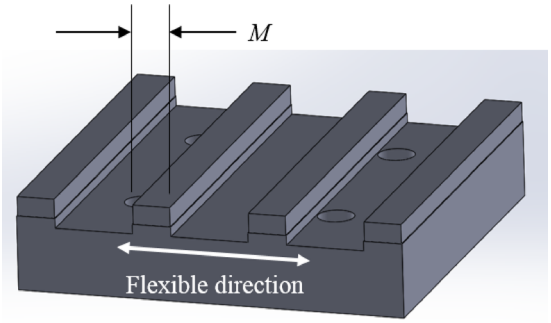

Fig. 34 The workpiece included four ribs that were initially machined to the same dimensions. The {5 mm axial depth, 2 mm radial depth} cuts were then performed on one edge at a different spindle speed for each rib. The SLE was calculated as the difference between the commanded, *C*, and measured, *M*, rib widths. The flexible direction for the flexure is identified.

spindle speed. Spindle speed values were selected to span from period-2 to stable cutting conditions while holding all other parameters constant. These spindle speeds and the corresponding behaviors are listed in Table 5.

The workpiece geometry is presented in Fig. 34. The initial ribs were machined directly on the flexure so it could be ensured that the part was aligned with the machine axes. Low axial and radial depths were selected to minimize vibration levels and the same conditions were used to machine each rib. Prior to beginning the SLE/Ra experiments, a test workpiece was machined and the four ribs were measured on a coordinate measuring machine, or CMM, to evaluate the repeatability of the starting rib dimensions (Zeiss Prismo). The mean value was 9.82 mm with a standard deviation of 2.8 μm. Given the adequate repeatability of the initial ribs, the 11 spindle speeds in Table 5 were used to machine 11 ribs (three total workpieces). All machining conditions were identical other than spindle speed.

Table 5 Spindle speeds and bifurcation behavior for experiments

Spindle speed (rpm)	Behavior
3180	Period-2
3190	Period-2
3200	Period-2
3210	Period-2
3270	Stable
3300	Stable
3330	Stable
3360	Stable
3400	Stable
3500	Stable
3600	Stable

The predicted and measured Poincaré maps for three of the 11 spindle speeds are presented in Figs. 35–37. Figure 35 displays the 3180 rpm results that exhibit period-2 behavior. Figures 36 and 37 both demonstrate stable behavior (3300 rpm and 3600 rpm, respectively). The vibration amplitude is larger in Fig. 37 because this spindle speed is nearer the first integer fraction of the resonant spindle speed (125.8(60)/2 = 7548/2 = 3774 rpm). The forced vibration amplitude is therefore increased. This would be considered a "best" spindle speed in traditional analyses because it identifies the peak of the corresponding secondary Hopf stability lobe.

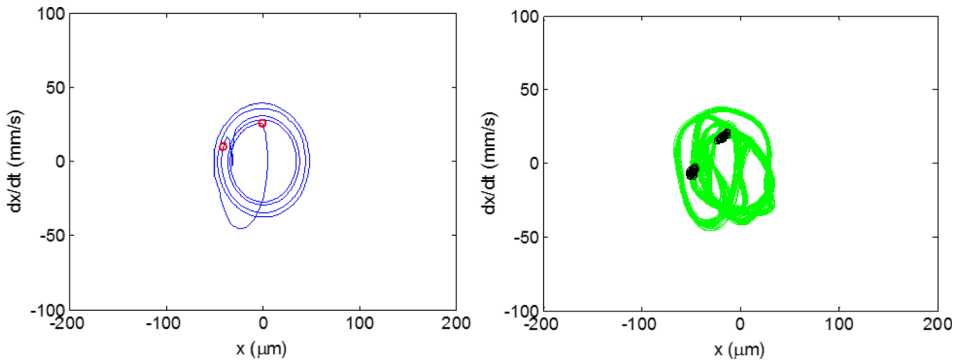

Fig. 35 Predicted (left) and measured (right) Poincaré maps for 3180 rpm. Period-2 behavior is seen. Note that *x* indicates the flexible direction for the flexure. The feed direction was *y* for these experiments.

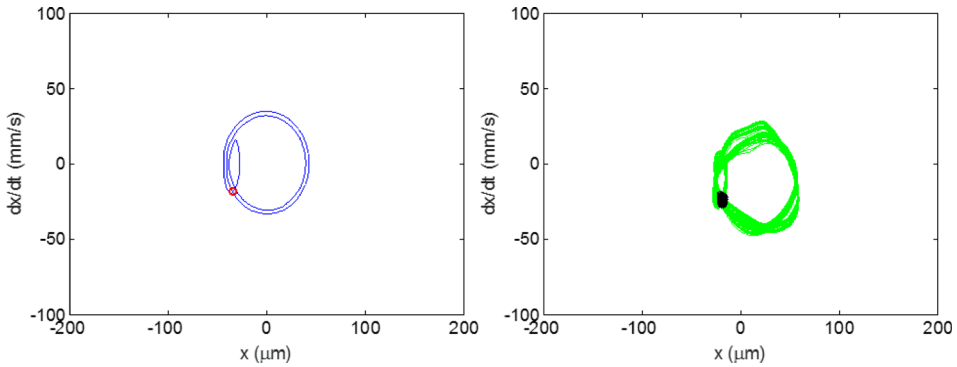

Fig. 36 Predicted (left) and measured (right) Poincaré maps for 3300 rpm. Stable behavior is seen.

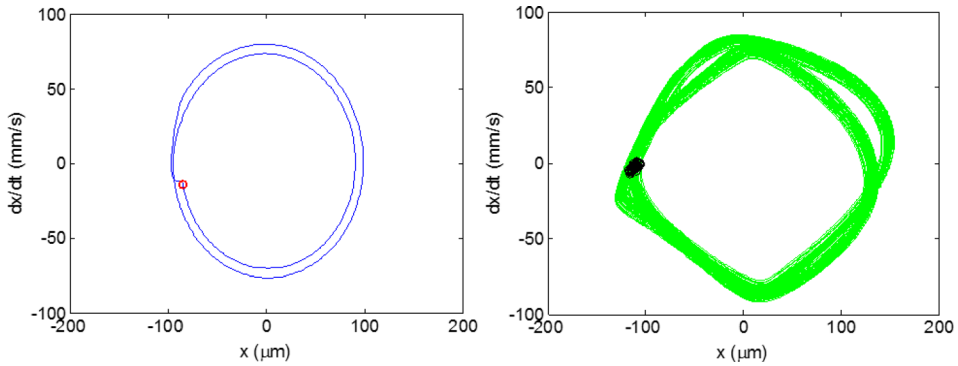

Fig. 37 Predicted (left) and measured (right) Poincaré maps for 3600 rpm. Stable behavior is seen with increased amplitude relative to 3300 rpm (Fig. 36).

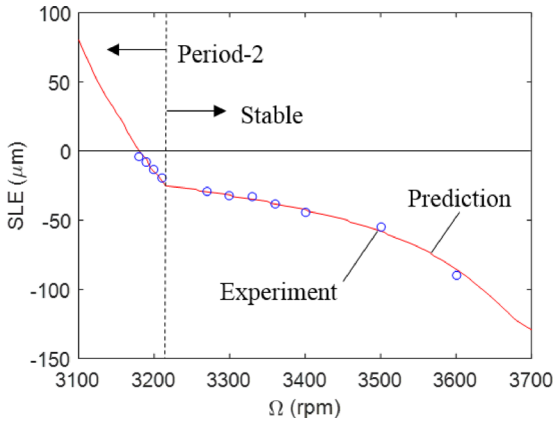

Fig. 38 Surface location error prediction from time domain simulation (line) and experimental results from rib cutting tests (circles). The four period-2 bifurcation tests are identified.

The SLE results are presented in Fig. 38. Four tests were completed under period-2 conditions and seven were performed under stable conditions. Good agreement is observed between prediction and measurement. The average error between prediction and measurement is 0.5 μm for the 11 tests.

The surface roughness was evaluated using both the CMM and a Zygo Zegage coherence scanning interferometer. Figures 39 and 40 provide a direct comparison between the time domain simulation and the CMM surface points obtained by continuous scanning along the machined surface. In these figures, the commanded surface is identified by the dashed line, the solid line is the CMM data, and the circles are the simulation results. The SLE is the difference between the commanded and actual surface and, again, good agreement is observed between simulation and measurement.

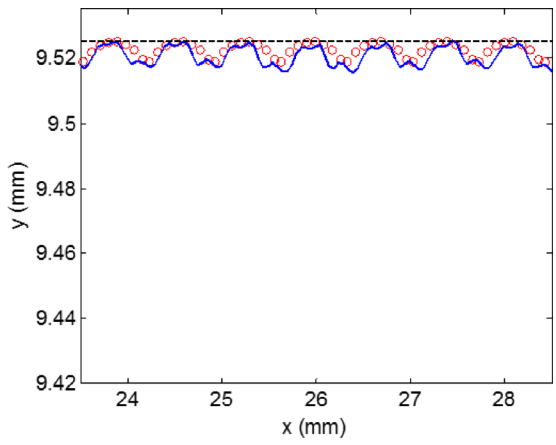

Fig. 39 Commanded surface (dashed line), CMM scan (solid line), and simulation result (circles) for 3180 rpm (period-2). These results correspond to Fig. 35.

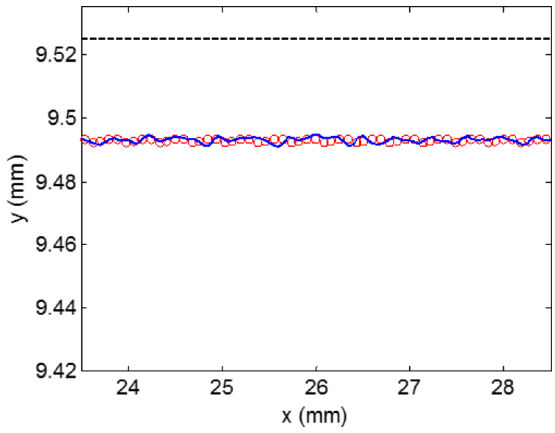

Fig. 40 Commanded surface (dashed line), CMM scan (solid line), and simulation result (circles) for 3300 rpm (stable). These results correspond to Fig. 36.

The coherence scanning interferometer results are presented in Table 6, where the Ra values were calculated from a line scan at the midpoint of the axial depth of cut extracted from the surface topography. The Ra is clearly larger for the period-2 conditions, where every other tool passage defines the surface roughness. The

Table 6 Surface roughness results for rib cutting tests

Spindle speed (rpm)	Behavior	Ra (μm)
3180	Period-2	1.76
3190	Period-2	1.77
3200	Period-2	1.87
3210	Period-2	2.09
3270	Stable	0.28
3300	Stable	0.35
3330	Stable	0.44
3360	Stable	0.34
3400	Stable	0.39
3500	Stable	0.36
3600	Stable	0.35

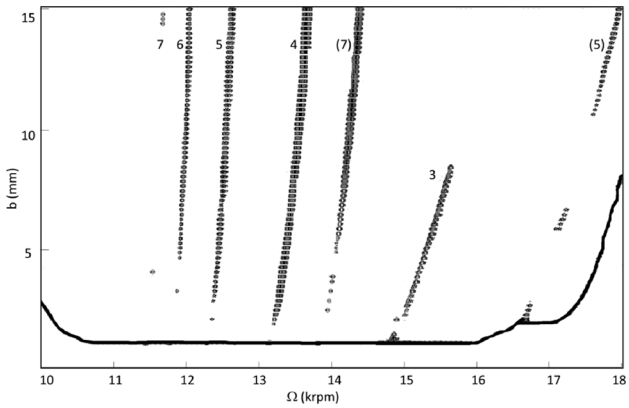

Fig. 41 Period-*n* bifurcation predictions for the rightmost stability lobe. The system dynamics are the same as those described in Section 4.7.

mean Ra for the period-2 conditions (four tests, 1.87 μm) is 5.2 times larger than the mean Ra for the stable conditions (seven tests, 0.36 μm).

6 High Spindle Speed Performance

A traditional stability lobe diagram was shown in Fig. 1. In this diagram, the chatter-free axial depth of cut for the rightmost stability lobe theoretically increases without limit as the spindle speed increases. Other than the work by Zatarain et al. [45], which suggested the period-2 closed islands of stability can appear even in the highest speed stability lobe for helical cutting edges, little attention has been paid to the presence or absence of period-*n* bifurcation behavior in this rightmost lobe. Using the validated time-domain simulation demonstrated here, this behavior was interrogated numerically. The system dynamics are the same as those presented in Sec. 4.7 (163 Hz natural frequency, which corresponds to a "best speed" of 9790 rpm for the left side of the rightmost stability lobe). The results are presented in Fig. 41, where Eq. (14) sampling strategy was applied with $n = 1, 2, 3, \ldots 7$. The same pattern observed in Fig. 32 emerges; note that the secondary Hopf bifurcation boundary is identified by a single solid line, rather than a dot at each simulation result.

7 Conclusions

Despite their relatively recent (1998) discovery, period-*n* bifurcations in milling have received significant attention in the literature. This review paper summarized: (1) these contributions; and (2) a three year investigation of the efficacy of selecting period-*n* behavior intentionally to produce machined parts. In this study, the presence of period-2 to period-15 bifurcations was predicted using time-domain simulation and validated experimentally. To aid in parameter selection that yields period-*n* behavior, graphical tools including Poincaré maps, bifurcation diagrams, and stability maps were presented. Additionally, the sensitivity to natural frequency and damping was evaluated. It was observed that the behavior can transition from secondary Hopf to period-*n* and vice versa as the natural frequency changes, but the machining parameters remain the same. It was also seen that increases in damping can reduce or eliminate the presence of the period-2 island within the traditional stable zone.

The question posed at the initiation of this comprehensive study was: *Can milling under period-n bifurcation conditions at axial depths of cut that exceed the traditional (secondary Hopf) stability limit be leveraged to achieve higher material removal rates, while still satisfying part accuracy and surface finish requirements?* Based on the simulation and experimental results, the practical answer is, yes, period-*n* conditions may be selected at axial depths of cut that exceed the secondary Hopf stability limit. The primary considerations for implementing this strategy are summarized.

- The SLE can be minimized by appropriate selection of spindle speed.
- The user must be willing to sacrifice surface quality due to the subharmonic (periodic) nature of the relative vibration between the cutting tool and workpiece. For this reason, the primary application may be roughing operations, where low surface roughness is not a primary requirement, which precede finishing operations under stable cutting conditions.
- Due to the sensitivity to natural frequency, this approach is best suited to situations where the workpiece is "rigid" relative to the cutting tool. Because the tool point dynamic response should remain constant throughout the cut for a selected spindle speed, consistent behavior should be achieved.

Based on these observations, the authors believe that it is possible for period-*n* behavior to be integrated in new milling process planning strategies that exploit the potential for increased material removal rates. Follow-on research to support this effort may focus on efficient techniques for presenting the global stability behavior in a map that incorporates both: (1) secondary Hopf and period-*n* bifurcation zones; and (2) surface location error. Additionally, the sensitivity of the period-*n* behavior to model input uncertainties can be quantified.

Funding Data

- Directorate for Engineering, National Science Foundation under Grant No. CMMI-1561221.

References

[1] Arnold, R. N., 1946, "The Mechanism of Tool Vibration in the Cutting of Steel," Proc. Inst. Mech. Eng., **154**(1), pp. 261–284.
[2] Doi, S., and Kato, S., 1956, "Chatter Vibration of Lathe Tools," Trans. ASME, **78**, 1956, p. 1127.
[3] Tobias, S., 1958, "The Chatter of Lathe Tools Under Orthogonal Cutting Conditions," Trans ASME, **80**, pp. 1079–1085.
[4] Tlusty, J., and Polacek, M., 1963, "The Stability of Machine Tools against Self-Excited Vibrations in Machining," ASME, pp. 465–474.
[5] Tobias, S. A., 1965, *Machine Tool Vibration*, Wiley, New York.
[6] Merritt, H. E., 1965, "Theory of Self-Excited Machine-Tool Chatter," ASME J. Eng. Ind., **87**(4), pp. 447–454.
[7] Tlusty, J., and Polacek, M., 1968, "Experience With Analysing Stability of Machine Tool against Chatter," 9th MTDR Conference, pp. 521–570.
[8] Shridar, R., Hohn, R. E., and Long, G. W., 1968, "A General Formulation of the Milling Process Equation," ASME J. Eng. Ind., **90**(2), pp. 317–324.
[9] Hohn, R. E., Shridar, R., and Long, G. W., 1968, "A Stability Algorithm for a Special Case of the Milling Process," ASME J. Eng. Ind., **90**(2), pp. 326–329.
[10] Shridar, R., Hohn, R. E., and Long, G. W., 1968, "A Stability Algorithm for the General Milling Process," ASME J. Eng. Ind., **90**(2), pp. 330–334.
[11] Hanna, N. H., and Tobias, S. A., 1974, "A Theory of Nonlinear Regenerative Chatter," J. Eng. Ind., **96**(1), pp. 247–255.
[12] Tlusty, J., and Ismail, F., 1981, "Basic Non-Linearity in Machining Chatter," Ann. CIRP, **30**(1), pp. 299–304.
[13] Tlusty, J., and Ismail, F., 1983, "Special Aspects of Chatter in Milling," ASME J. Vib., Stress Reliab. Des., **105**(1), pp. 24–32.
[14] Tlusty, J., 1985, "Machine Dynamics," *Handbook of High-Speed Machining Technology*, R. I., King, ed., Chapman and Hall, New York, pp. 48–153.
[15] Tlusty, J., 1986, "Dynamics of High-Speed Milling," ASME J. Eng. Ind., **108**(2), pp. 59–67.
[16] Minis, I., and Yanusevsky, R., 1993, "A New Theoretical Approach for Prediction of Chatter in Milling," ASME J. Eng. Ind., **115**(1), pp. 1–8.
[17] Altintas, Y., and Budak, E., 1995, "Analytical Prediction of Stability Lobes in Milling," Ann. CIRP, **44**(1), pp. 357–362.
[18] Altintas, Y., and Weck, M., 2004, "Chatter Stability of Metal Cutting and Grinding," Ann. CIRP, **53**(2), pp. 619–642.
[19] Davies, M. A., Dutterer, B. S., Pratt, J. R., and Schaut, A. J., 1998, "On the Dynamics of High-Speed Milling With Long, Slender Endmills," Ann. CIRP, **47**(1), pp. 55–60.
[20] Moon, F. C., and Kalmár-Nagy, T., 2001, "Nonlinear Models for Complex Dynamics in Cutting Materials," Philos. Trans. R. Soc. London A, **359**(1781), pp. 695–711.
[21] Davies, M. A., Pratt, J. R., Dutterer, B. S., and Burns, T. J., 2000, "The Stability of Low Radial Immersion Milling," Ann. CIRP, **49**(1), pp. 37–40.

[22] Moon, F. C., 1994, "Chaotic Dynamics and Fractals in Material Removal Processes," *Nonlinearity and Chaos in Engineering Dynamics*, J. Thompson, and S. Bishop, eds., pp Wiley, New York, pp. 25–37.
[23] Bukkapatnam, S., Lakhtakia, A., and Kumara, S., 1995, "Analysis of Senor Signals Shows Turning on a Lathe Exhibits Low-Dimensional Chaos," Phys. Rev. E, **52**(3), pp. 2375–2387.
[24] Stépán, G., and Kalmár-Nagy, T., 1997, "Nonlinear Regenerative Machine Tool Vibrations," ASME Paper No. DETC 97/VIB-4021.
[25] Nayfey, A., Chin, C., and Pratt, J., 1998, "Applications of Perturbation Methods to Tool Chatter Dynamics," *Dynamics and Chaos in Manufacturing Processes*, F. C. Moon, ed., Wiley, New York, pp. 193–213.
[26] Minis, I., and Berger, B. S., 1998, "Modelling, Analysis, and Characterization of Machining Dynamics," *Dynamics and Chaos in Manufacturing Processes*, F. C. Moon, ed., Wiley, New York, pp. 125–163.
[27] Moon, F. C., and Johnson, M., 1998, "Nonlinear Dynamics and Chaos in Manufacturing Processes," *Dynamics and Chaos in Manufacturing Processes*, F. C. Moon, ed., Wiley, New York, pp. 3–32.
[28] Smith, K. S., and Tlusty, J., 1991, "An Overview of Modeling and Simulation of the Milling Process," J. Eng. Ind., **113**(2), pp. 169–175.
[29] Campomanes, M. L., and Altintas, Y., 2003, "An Improved Time Domain Simulation for Dynamic Milling at Small Radial Immersions," ASME J. Manuf. Sci. Eng., **125**(3), pp. 416–422.
[30] Zhao, M. X., and Balachandran, B., 2001, "Dynamics and Stability of Milling Process," Int. J. Solids Struct., **38**(10–13), pp. 2233–2248.
[31] Davies, M. A., Pratt, J. R., Dutterer, B., and Burns, T. J., 2002, "Stability Prediction for Low Radial Immersion Milling," ASME J. Manuf. Sci. Eng., **124**(2), pp. 217–225.
[32] Mann, B. P., Insperger, T., Bayly, P. V., and Stépán, G., 2003, "Stability of Up-Milling and Down-Milling—Part 2: Experimental Verification," Int. J. Mach. Tools Manuf., **43**(1), pp. 35–40.
[33] Mann, B. P., Insperger, T., Bayly, P. V., and Stépán, G., 2003, "Stability of Up-Milling and down-Milling—Part 1: Alternative Analytical Methods," Int. J. Mach. Tools Manuf., **43**(1), pp. 25–34.
[34] Insperger, T., Stépán, G., Bayly, P. V., and Mann, B. P., 2003, "Multiple Chatter Frequencies in Milling Processes," J. Sound Vib., **262**(2), pp. 333–345.
[35] Insperger, T., and Stépán, G., 2004, "Vibration Frequencies in High-Speed Milling Processes or a Positive Answer to Davies, Pratt, Dutterer, and Burns," ASME J. Manuf. Sci. Eng., **126**(3), pp. 481–487.
[36] Mann, B. P., Bayly, P. V., Davies, M. A., and Halley, J. E., 2004, "Limit Cycles, Bifurcations, and Accuracy of the Milling Process," J. Sound Vib., **277**(1–2), pp. 31–48.
[37] Merdol, S. D., and Altintas, Y., 2004, "Multi Frequency Solution of Chatter Stability for Low Immersion Milling," J. Manuf. Sci. Eng., **126** (3), pp. 459–466.
[38] Govekar, E., Gradišek, J., Kalveram, M., Insperger, T., Weinert, K., Stépán, G., and Grabec, I., 2005, "On Stability and Dynamics of Milling at Small Radial Immersion. Annals of the," CIRP, **54**(1), pp. 357–362.
[39] Gradišek, J., Kalveram, M., Insperger, T., Weinert, K., Stépán, G., Govekar, E., and Grabec, I., 2005, "On Stability Prediction for Milling," Int. J. Mach. Tools Manuf., **45**(1), pp. 769–781.
[40] Budak, E., and Altintas, Y., 1998, "Analytical Prediction of Chatter Stability in Milling Part I: General Formulation," ASME J. Dyn. Syst., Meas., Control, **120**(1), pp. 22–30.
[41] Budak, E., and Altintas, Y., 1998, "Analytical Prediction of Chatter Stability in Milling Part II: Application of the General Formulation to Common Milling Systems," ASME J. Dyn. Syst., Meas., Control, **120**(1), pp. 31–36.
[42] Altintas, Y., Stepan, G., Merdol, D., and Dombovari, Z., 2008, "Chatter Stability of Milling in Frequency and Discrete Time Domain," CIRP J. Manuf. Sci. Technol., **1**(1), pp. 35–44.
[43] Mann, B. P., Garg, N. K., Young, K. A., and Helvey, A. M., 2005, "Milling Bifurcations From Structural Asymmetry and Nonlinear Regeneration," Nonlinear Dyn., **42**(4), pp. 319–337.
[44] Stépán, G., Szalai, R., Mann, B. P., Bayly, P. V., Insperger, T., Gradisek, J., and Govekar, E., 2005, "Nonlinear Dynamics of High-Speed Milling—Analyses, Numerics, and Experiments," ASME J. Vib. Acoust., **127**(2), pp. 197–203.
[45] Zatarain, M., Muñoa, J., Peigné, G., and Insperger, T., 2006, "Analysis of the Influence of Mill Helix Angle on Chatter Stability," Ann. CIRP, **55**(1), pp. 365–368.
[46] Insperger, T., Munoa, J., Zatarain, M. A., and Peigné, G., 2006, "Unstable Islands in the Stability Chart of Milling Processes Due to the Helix Angle," CIRP Second International Conference on High Performance Cutting, Vancouver, BC, Canada, June 12–13.
[47] Patel, B. R., Mann, B. P., and Young, K. A., 2008, "Uncharted Islands of Chatter Instability in Milling," Int. J. Mach. Tools Manuf., **48**(1), pp. 124–134.
[48] Bobrenkov, O. A., Khasawneh, F. A., Butcher, E. A., and Mann, B. P., 2010, "Analysis of Milling Dynamics for Simultaneously Engaged Cutting Teeth," J. Sound Vib., **329**(5), pp. 585–606.
[49] Moradi, H., Vossoughi, G., and Movahhedy, M., 2014, "Bifurcation Analysis of Nonlinear Milling Process With Tool Wear and Process Damping: Sub-Harmonic Resonance Under Regenerative Chatter," Int. J. Mech. Sci., **85**, pp. 1–19.
[50] Cheng, C., Wang, Z., Hung, W., Bukkapatnam, S., and Komanduri, R., 2015, "Ultra-Precision Machining Process Dynamics and Surface Quality Monitoring," Procedia Manuf., **1**, pp. 607–618.
[51] Honeycutt, A., and Schmitz, T., 2015, "The Extended Milling Bifurcation Diagram," Procedia Manuf., **1**, pp. 466–476.
[52] Honeycutt, A., and Schmitz, T., 2016, "A Numerical and Experimental Investigation of Period-n Bifurcations in Milling," ASME J. Manuf. Sci. Eng., **139**(1), p. 011003.
[53] Honeycutt, A., and Schmitz, T., 2016, "Experimental Validation of Period-n Bifurcations in Milling," Procedia Manuf., **5**, pp. 362–374.
[54] Honeycutt, A., and Schmitz, T., 2016, "A New Metric for Automated Stability Identification in Time Domain Milling Simulation," ASME J. Manuf. Sci. Eng., **138**(7), p. 074501.
[55] Honeycutt, A., and Schmitz, T., 2017, "Milling Stability Interrogation by Sub-harmonic Sampling," ASME J. Manuf. Sci. Eng., **139**(4), p. 041009.
[56] Schmitz, T., and Smith, K. S., 2009, *Machining Dynamics: Frequency Response to Improved Productivity*, Springer, New York.
[57] Kline, W., DeVor, R., and Shareef, I., 1982, "The Prediction of Surface Accuracy in End Milling," J. Eng. Ind., **104**(3), pp. 272–278.
[58] Kline, W., DeVor, R., and Lindberg, J., 1982, "The Prediction of Cutting Forces in End Milling With Application to Cornering Cuts," Int. J. Mach. Tool Des. Res., **22**(1), pp. 7–22.
[59] Tlusty, J., 1985, "Effect of End Milling Deflections on Accuracy," *Handbook of High Speed Machining Technology*, R. I. King ed., Chapman and Hall, New York, pp. 140–153.
[60] Sutherland, J., and DeVor, R., 1986, "An Improved Method for Cutting Force and Surface Error Prediction in Flexible End Milling Systems," J. Eng. Ind., **108**(4), pp. 269–279.
[61] Montgomery, D., and Altintas, Y., 1991, "Mechanism of Cutting Force and Surface Generation in Dynamic Milling," J. Eng. Ind., **113**(2), pp. 160–168.
[62] Altintas, Y., Montgomery, D., and Budak, E., 1992, "Dynamic Peripheral Milling of Flexible Structures," J. Eng. Ind., **114**(2), pp. 137–145.
[63] Tarng, Y., Liao, C., and Li, H., 1994, "A Mechanistic Model for Prediction of the Dynamics of Cutting Forces in Helical End Milling," Int. J. Model. Simul., **14**(2), pp. 92–97.
[64] Schmitz, T., and Ziegert, J., 1999, "Examination of Surface Location Error Due to Phasing of Cutter Vibrations," Precis. Eng., **23**(1), pp. 51–62.
[65] Altintas, Y., 2000, *Manufacturing Automation*, Cambridge University Press, Cambridge, UK.
[66] Schmitz, T., Couey, J., Marsh, E., Mauntler, N., and Hughes, D., 2007, "Runout Effects in Milling: Surface Finish, Surface Location Error, and Stability," Int. J. Mach. Tools Manuf., **47**(5), pp. 841–851.
[67] Yun, W.-S., Ko, J., Cho, D.-W., and Ehmann, K., 2002, "Development of a Virtual Machining System, Part 2: Prediction and Analysis of a Machined Surface Error," Int. J. Mach. Tools Manuf., **42**(15), pp. 1607–1615.
[68] Schmitz, T., and Mann, B., 2006, "Closed-Form Solutions for Surface Location Error in Milling," Int. J. Mach. Tools Manuf., **46**(12–13), pp. 1369–1377.
[69] Dombovari, Z., and Stépán, G., 2015, "On the Bistable Zone of Milling Processes," Philos. Trans. R. Soc. A, **373**(2051), p. 20140409.
[70] Bachrathy, D., Munoa, J., and Stépán, G., 2016, "Experimental Validation of Appropriate Axial Immersions for Helical Mills," Int. J. Adv. Manuf. Technol., **84**(5–8), pp. 1295–1302.
[71] Honeycutt, A., and Schmitz, T., 2017, "A Study of Milling Surface Quality During Period-2 Bifurcations," Procedia Manuf., **10**, pp. 183–193.
[72] Ransom, T., Honeycutt, A., and Schmitz, T., 2016, "A New Tunable Dynamics Platform for Milling Experiments," Precis. Eng., **44**, pp. 252–256.